

UNIVERSITY OF THE WESTERN CAPE

# Investigating the Gamma-ray Strength Function in $^{74}\text{Ge}$ using the Ratio Method

by

Khanyisa Sowazi

A thesis submitted in partial fulfillment of  
the requirements for the degree of  
Master of Science

in the

Department of Physics

University of the Western Cape

Supervisor: Dr Mathis Wiedeking

Co-supervisor: Prof. Jose Nicolas Orce-Gonzalez

July 26, 2018

# Keywords

- $\gamma$  ray strength function
- $(n,\gamma)$  cross sections
- Add-back
- Banana Spectra
- Branching Ratio
- Brink-axel hypothesis
- Low Energy Enhancement
- Multipolarity
- Nuclear level density
- Particle- $\gamma$  coincidence
- Particle ray tracing
- Primary  $\gamma$  rays
- Quasi-continuum
- Quasi strength
- Ratio Method



# Abstract

## Investigating the Gamma-ray Strength Function in $^{74}\text{Ge}$ using the Ratio Method

K. Sowazi

MSc Thesis, Department of Physics, University of the Western Cape

An increasing number of measurements reveal the presence of a low-energy enhancement in the gamma-ray strength function (GSF). The GSF, which is the ability of nuclei to absorb or emit  $\gamma$  rays, provides insight into the statistical properties of atomic nuclei. For this project the GSF was studied for  $^{74}\text{Ge}$  which was populated in the reaction  $^{74}\text{Ge}(p,p')^{74}\text{Ge}^*$  at a beam energy of 18 MeV. The data were collected with the STARS-LIBERACE array at Lawrence Berkeley National Laboratory. Silicon detector telescopes were used for particle identification and  $\gamma$  rays in coincidence were detected with 5 clover-type high-purity germanium detectors. Through the analysis particle- $\gamma$ - $\gamma$  coincidence events were constructed. These events, together with well-known energy levels, were used to identify primary  $\gamma$  rays from the quasicontinuum. Primary  $\gamma$  rays from a broad excitation energy region, which decay to six  $2^+$  states could be identified. These states and the associated primary  $\gamma$  rays are used to measure the GSF for  $^{74}\text{Ge}$  with the Ratio Method [1], which entails taking ratios of efficiency-corrected primary  $\gamma$ -ray intensities from the quasicontinuum. Results from the analysis of the data and focus on the existence of the low-energy enhancement in  $^{74}\text{Ge}$  will be discussed. The results are further discussed in the context of other work done on  $^{74}\text{Ge}$  using the  $(\gamma,\gamma')$  [2],  $(^3\text{He},^3\text{He}')$  [3] and  $(\alpha,\alpha')$  [4] reactions.

July 26, 2018

# Declaration



I, Khanyisa Sowazi, declare that *Investigating the Gamma-ray Strength Function in  $^{74}\text{Ge}$  using the Ratio Method* is my own work, that it has not been submitted for any degree or examination in any other university, and that all the sources I have used or quoted have been indicated and acknowledged by complete references.

Full name: .....

Signature: .....

Date: .....



# Dedication

I would like to dedicate this work to my late father Tembile Mazitshana for the self discipline that he has instilled in me. For teaching me to be respectful and humble. His contagious love for education spread in me. I am sure he would be very proud of me right now if he was here. He showed me that nothing is more important than family and I hope to carry that tradition into my own family too.



# Acknowledgements

I would like to humbly acknowledge my supervisor Dr Mathis Wiedeking to whom without this project would not be possible. He has been very supportive throughout my masters project and made my learning process very pleasurable. I thank him for allowing me the opportunity to visit CERN on the experiment we conducted at ISOLDE in November 2016. I learned a lot from the trip and gained a lot of experience in the two weeks that we spent there that will help me for my entire scientific life.

I would like to thank NRF for fully funding my MSc project and sponsoring all my trips and conferences that I had to attend. Without NRF's financial support, this project would have not come into existence. I would also like to thank iThemba LABS for giving me the perfect office to carry out my project, the ever so reliable internet and experience they have given me through the AFRODITE experiments that were running on weekends.

I would like to express my deep appreciation to my best friend and girlfriend Anelisa Tomsana for the outstanding care, encouragement and support that she has given me throughout this journey. She was the person I could go to whenever work felt too overwhelming and was able to make me feel better. I am deeply thankful for her understanding when I had to be at the laboratory up until late and even through the weekends and understanding when I had to go out of country.

I would like to thank my aunt Ntombine Mazitshana who is my legal guardian, but most importantly a mother figure, for grooming me into the man I am today and for allowing me to further my education. I would like to thank my aunt Nosithembiso Mazitshana for the support, motivation she has given me and for her belief in me that she has never shied from showing me. I would like to show appreciation to aunt Xoliswa Tempi for her encouragement and warmth throughout my journey up until now.

I am abidingly grateful to Ayanda Kunyana for his helpful good heart and humanity that he has shown me. I would also like to extend my gratitude to Samkelo Tempa for contributing to my journey, Nosiphiwe Mkhala for being a big sister and for motivating me all these years to keep studying, and achieve what our family could not achieve and lastly thank Phumelele Tempa for the support and inspiration that he kept giving me. His excitement over my achievements gave me the drive to keep working hard.



*“Education helps one cease being intimidated by strange situations.”*

Maya Angelou

*“There are risks and costs to a program of action. But they are far less than the long-range risks and costs of comfortable inaction.”*

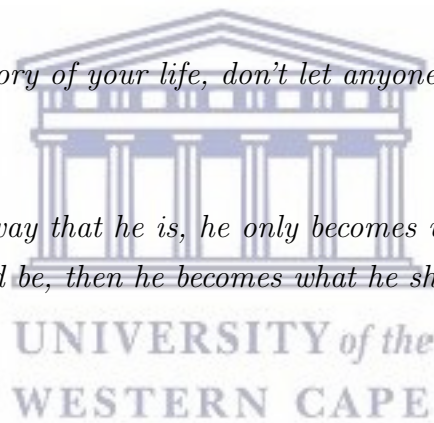
John F. Kennedy

*“When writing the story of your life, don’t let anyone else hold the pen.”*


Harley Davidson

*“Look at a man the way that he is, he only becomes worse. But look at him as if he were what he could be, then he becomes what he should be.”*

Goethe



# Contents

Keywords	i
Abstract	ii
Declaration of Authorship	iii
Dedication	iv
Acknowledgements	v
List of Figures	x
List of Tables	xiii
Abbreviations	xiv
	
<b>1 Introduction</b>	<b>1</b>
1.1 Background . . . . .	1
1.2 Motivation . . . . .	5
1.3 Research Questions . . . . .	7
1.4 Thesis Outline . . . . .	8
<b>2 Theory and literature review</b>	<b>9</b>
2.1 $\gamma$ -ray Strength Function . . . . .	9
2.2 Level Density . . . . .	11
2.2.1 Back-shifted Fermi Gas model . . . . .	11
2.2.2 Constant Temperature model . . . . .	12
2.3 $\gamma$ -ray Cascade from Quasi-continuum . . . . .	13
2.4 The Giant Dipole Resonance (GDR) . . . . .	14
2.4.1 The Pygmy and Scissors Resonances . . . . .	17
2.5 $\gamma$ -ray Strength Function and Cross sections . . . . .	18

2.6	The Ratio Method . . . . .	19
<b>3</b>	<b>Experimental Techniques</b>	<b>22</b>
3.1	Details of the experiment . . . . .	22
3.2	High Purity Germanium Detectors . . . . .	22
3.3	Silicon Detector Telescope (SDT) . . . . .	25
3.4	Signal Processing . . . . .	27
3.5	Calibration of data . . . . .	29
<b>4</b>	<b>Analysis</b>	<b>34</b>
4.1	Software For Sorting and Displaying Histograms . . . . .	34
4.2	Particle Analysis . . . . .	36
4.3	Energy Corrections . . . . .	42
4.4	$\gamma$ -ray Analysis . . . . .	46
4.5	Efficiency Calibration for HPGe Detector . . . . .	50
4.6	Results . . . . .	52
<b>5</b>	<b>Discussion</b>	<b>56</b>
5.1	Ratios . . . . .	56
5.2	Conclusion . . . . .	61
<b>Bibliography</b>		<b>65</b>



# List of Figures

1.1	An edited image showing the report <i>Connecting Quarks with the Cosmos</i> published in 2003 and the 11 important questions in astronomy and physics [6] originating from [5]. . . . .	1
1.2	A schematic representation of the binding energy per nucleon of different elements [7]. . . . .	2
1.3	A schematic representation of the p, r and s-process [8]. . . . .	3
1.4	Ratios of Maxwellian-averaged $(n, \gamma)$ reaction rates at $T = 10^9 K$ for the Fe, Mo, and Cd isotopic chains up to the neutron drip line, using the generalized Lorentzian (GLO) model [13]. . . . .	5
1.5	The $\gamma$ -ray strength function of $^{74}\text{Ge}$ from the reaction $^{74}\text{Ge}(^3\text{He}, ^3\text{He}')^{74}\text{Ge}^*$ , showing the low energy enhancement [3]. . . . .	6
2.1	A schematic of statistical $\gamma$ -rays originating from the quasi-continuum region. . . . .	10
2.2	A schematic representation of the $\gamma$ -ray cascade method used to construct the strength functions. . . . .	14
2.3	The Giant Dipole Resonance. . . . .	16
2.4	A qualitative scheme of giant resonance modes of the nucleus, courtesy of [12]. . . . .	16
2.5	The schematic of the Giant Dipole Resonance with the Pygmy and Scissors resonances. . . . .	18
2.6	A schematic representation of how the primary $\gamma$ rays are extracted for the ratios. (i) <i>Gates are applied to different excited states on the proton spectra.</i> (ii) <i>How the gates apply to the energy level scheme of the <math>^{74}\text{Ge}</math> nucleus.</i> (iii) <i>After the proton gate, a <math>\gamma</math> ray gate is applied to a well known low lying state.</i> (iv) <i>A primary <math>\gamma</math> ray is required such that when one adds it up to the lower lying <math>\gamma</math> ray, they add-up to the total excitation energy defined by the proton gate.</i> . . . .	20
3.1	The clover detectors used for $\gamma$ -ray detection [24]. . . . .	23
3.2	Energy band gap schematic showing the structure of metals, semiconductors and insulators [25]. . . . .	24
3.3	The Silicon Detector Telescope (SDT) used for proton detection [24]. . . . .	25
3.4	A schematic representation of the silicon setup. . . . .	26
3.5	A schematic representation of analogue electronics setup. . . . .	27

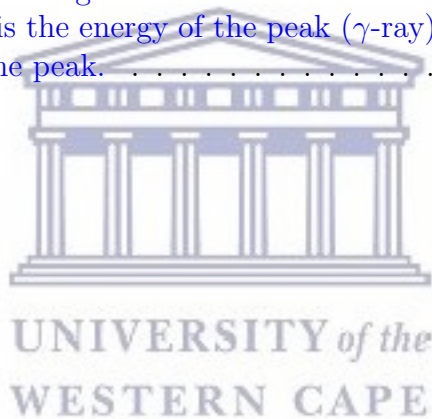
3.6	A schematic representation of time gates on the Silicon Detector Telescope. So the time logic signals constitute a singles event since the second signal comes within a space of less than 100 ns after the first one, while the second is not an event since the second signal comes after the required 100 ns gap. . . . .	28
3.7	The six spectra from $^{74}\text{Ge}$ after calibration was performed. All the energy peaks are correctly overlaid on top of each other. . . . .	30
3.8	An example of the spectra of $^{226}\text{Ra}$ that was used for calibration. . . . .	31
3.9	A schematic representation of the decay chain of $^{226}\text{Ra}$ [28]. The four dashed ellipsoids represent the four last peaks observed in figure 3.8. . . . .	32
3.10	A representation of the time spectra before spectral alignment and add-back as read by the data acquisition system from the TDC. . . . .	33
3.11	A representation of the time spectrum after all single time spectra are aligned and add-back is completed. . . . .	33
4.1	A step by step schematic representation of how the software work together to create histograms and matrix plots that are used for the analysis. . . . .	35
4.2	A schematic example of an S2 Silicon Detector. . . . .	36
4.3	Schematic of particle ray tracing performed on the Silicon Detector Telescope. . . . .	37
4.4	The sector count spectra created from each interaction with the SDT. The figure on the left (A) shows the events before charged particle ray tracing while the one on the right (B) shows the events after charged particle ray tracing. . . . .	38
4.5	The ring count spectra created from each interaction with the SDT. The map shown in (A) is before charged particle ray tracing and the one shown in (B) is after charged particle tracing. . . . .	38
4.6	Schematic of energy sharing correction in adjacent rings. . . . .	39
4.7	2-D spectra for back sector energies against front sector energies. . . . .	40
4.8	2-D spectra for back ring energies against front ring energies. . . . .	41
4.9	Particle- $\gamma$ gated banana spectra for sectors. (A) is the spectra before the banana gates to suppress all the other channels besides $^{74}\text{Ge}(p,p')^{74}\text{Ge}$ and punch through. (B) is the spectra after the suppression is done and only the $^{74}\text{Ge}(p,p')^{74}\text{Ge}$ channel is visible. . . . .	42
4.10	Schematic of the recoil correction for aluminum foil. . . . .	43
4.11	Two body kinematics of a proton projectile and a $^{74}\text{Ge}$ nucleus. . . . .	44
4.12	Energy spectrum from $^{74}\text{Ge}(p,p')^{74}\text{Ge}$ reaction . . . . .	46
4.13	Excitation energies after recoil and aluminum foil energy loss corrections up to 2 MeV. The peak with the highest counts is the 596 keV $\gamma$ -ray which belongs to the first excited state of the nucleus. . . . .	47
4.14	Particle versus $\gamma$ -ray energy spectra. . . . .	48



4.15	A schematic representation of how particle- $\gamma$ - $\gamma$ coincidences are done. A gate in excitation energy at the quasi-continuum is applied, followed by a gate on a secondary $\gamma$ -ray that decays to the ground state. A primary $\gamma$ -ray is required to come from the quasi-continuum and feed into the state of the secondary $\gamma$ , which is the 596 keV level state in this case. . . . .	49
4.16	The primary $\gamma$ -rays that are coming out of the quasi-continuum and feeding directly into the 596 keV state. . . . .	49
4.17	Two $\gamma$ -rays that were used for efficiency calibration coming from $^{14}\text{C}$ . The spectrum shows the energy range between 2 and 8 MeV. . . . .	51
4.18	Three $\gamma$ -rays that were used for efficiency calibration coming from $^{13}\text{C}$ . . . . .	51
4.19	An efficiency plot for all the HPGe detectors which was measured from $^{152}\text{Eu}$ , $^{13}\text{C}$ and $^{14}\text{C}$ . . . . .	53
5.1	A schematic diagram of the branching ratio of the 1204 keV level decaying to the 596 keV and ground state. . . . .	56
5.2	Ratios $R = f(E_{596})/f(E_{1204})$ for primary $\gamma$ -rays that feed into the 596 keV state over those that feed into the 1204 keV state. . . . .	57
5.3	The ratios of the strength of primary $\gamma$ -rays that are feeding into the 596 keV state against the strength of the primary $\gamma$ -rays that are feeding into the 1204 keV state. . . . .	59
5.4	The shape of the GSF as depicted by the ratios. . . . .	59
5.5	The shape of the strength function for $R < 1$ . . . . .	60
5.6	A plot of the data from the reaction $^{74}\text{Ge}(^3\text{He}, ^3\text{He}^*)^{74}\text{Ge}$ , taken from Ref [3]. The actual data on the plot are represented by the purple line, the red line is the upper uncertainty limit and the green one is the lower uncertainty limit. . . . .	61
5.7	A plot of the data from figure 5.3 in brown and the data from figure 5.6 in blue. . . . .	62
5.8	A plot of the data from figure 5.3 in brown and the Oslo data in blue rebinned with the use of a polynomial fit of order 2. . . . .	63
5.9	The experimental level density of $^{74}\text{Ge}$ from Ref. [3]. The arrows show where the Oslo data joins the Back-shifted Fermi gas model and at the discrete energy levels. . . . .	64

# List of Tables

3.1	The table shows the experimental data of $\gamma$ -ray energies retrieved from National Nuclear Data Center (NNDC) website [27], which were used to calibrate the data. . . . .	29
3.2	The table of proton energy calibration. $^{226}\text{Ra}$ alpha source was used for the calibration, where the second column shows the channel values and the third column shows the corresponding energy values taken from NNDC [27]. . . . .	30
4.1	$^{14}\text{C}$ transition anergies that were used for efficiency calibration. The first column is the energy of the peak ( $\gamma$ -ray) and the second is the area under the peak. . . . .	50



# Abbreviations

<b>HPGe</b>	<b>H</b> igh <b>P</b> urity <b>G</b> ermanium.
<b>SDT</b>	<b>S</b> ilicon <b>D</b> etector <b>T</b> elescope.
<b>NLD</b>	<b>N</b> uclear <b>L</b> evel <b>D</b> ensity.
<b>CAMAC</b>	<b>C</b> omputer- <b>A</b> ided <b>M</b> easurement <b>A</b> nd <b>C</b> ontrol.
<b>BGO</b>	<b>B</b> ismuth <b>G</b> ermanate <b>O</b> xide.
<b>STARS</b>	<b>S</b> ilicon <b>T</b> elescope <b>A</b> rray for <b>R</b> eaction <b>S</b> tudies.
<b>LiBerACE</b>	<b>L</b> ivermore <b>B</b> erkeley <b>A</b> rray for <b>C</b> ollaborative <b>E</b> xperiments.
<b>LEE</b>	<b>L</b> ow <b>E</b> nergy <b>E</b> nhancement.
<b>GSF</b>	<b>G</b> amma-ray <b>S</b> trength <b>F</b> unction.



UNIVERSITY *of the*  
WESTERN CAPE

# Chapter 1

## Introduction

### 1.1 Background

In the report, *Connecting Quarks with the Cosmos: Eleven Science Questions for the New Century*, published in 2003 [5], 11 questions from both astronomy and physics were discussed. These questions are at the interface of both these fields.

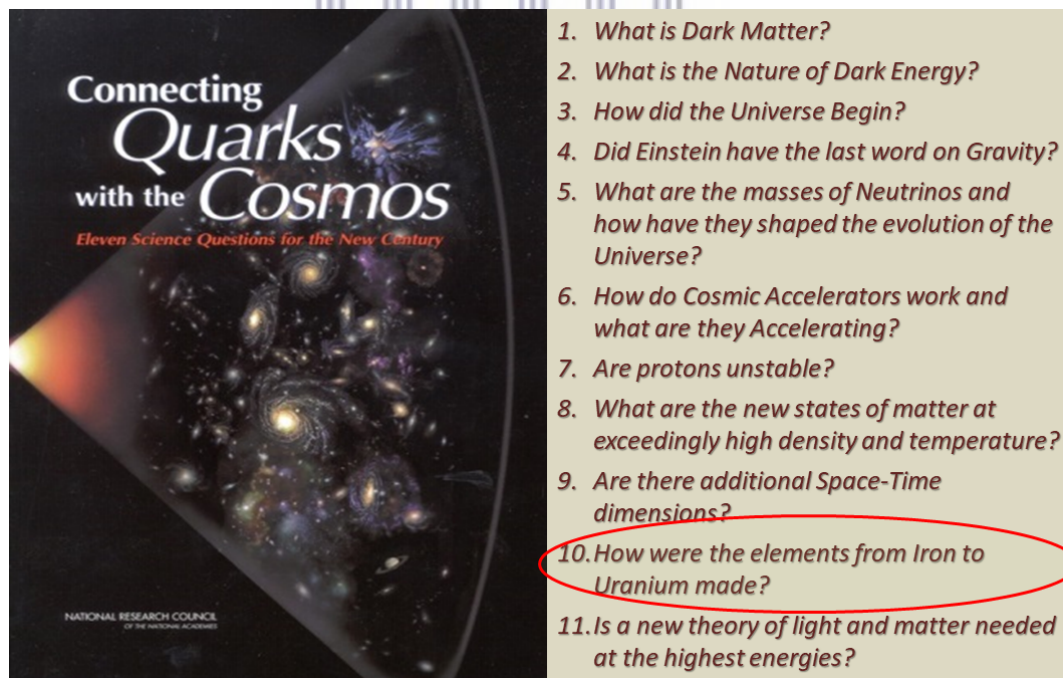


FIGURE 1.1: An edited image showing the report *Connecting Quarks with the Cosmos* published in 2003 and the 11 important questions in astronomy and physics [6] originating from [5].

This report identifies these 11 key questions that have a good chance of being

answered if the different fields of science collaborate together, which are listed in figure 1.1. Out of the 11 questions, this project concerns itself with question 10, *How were the elements from Iron to Uranium made?* To try and answer this question, one first needs to understand how elements lighter than iron are created and why those that are heavier than iron are not synthesized in the same way as those that are lighter than iron. Nuclei from  $^1\text{H}$  up to  $^{56}\text{Fe}$  undergo nuclear fusion in stars, while those from  $^{63}\text{Cu}$  up to  $^{238}\text{U}$  clearly cannot as they would consume more energy than they give off, as follows from Einstein's equation  $E = \Delta mc^2$ .

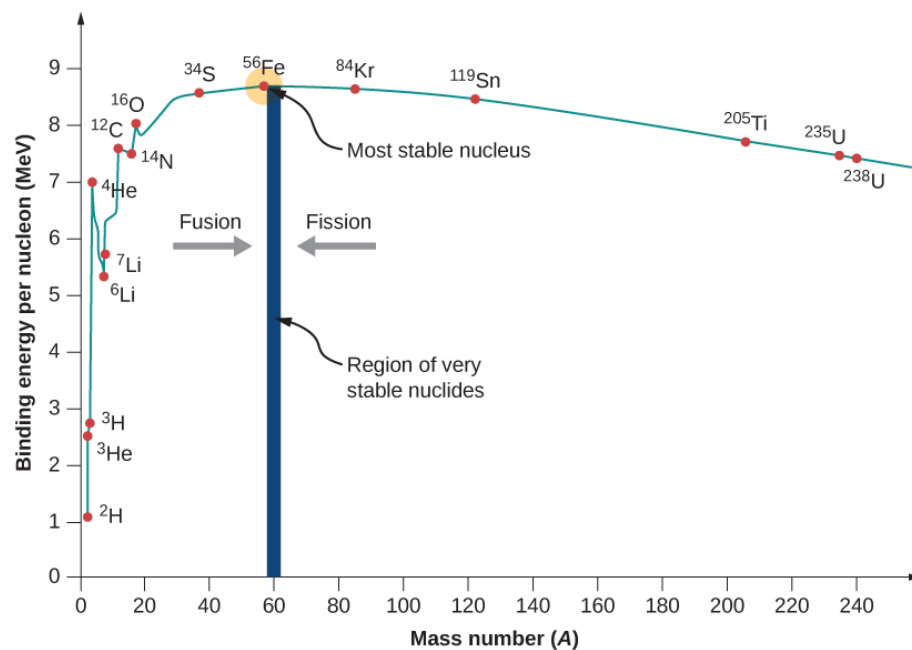


FIGURE 1.2: A schematic representation of the binding energy per nucleon of different elements [7].

Figure 1.2 shows the binding energies of different nuclei, and the most interesting part of the distribution is at the maximum. Here are the elements with the highest binding energy per nucleon. This means that for nuclear fusion from hydrogen up to the maximum point, there is more energy released than is consumed in the reaction and after this maximum, more energy is consumed than is released. In short this means that nuclear fusion is unlikely in astrophysical settings that produce elements heavier than iron, hence the elements from copper up to uranium must be created from different processes.

Some of the proposed processes include the absorption of neutrons in the astrophysical environments through two reaction synthesis, namely the r-process

and s-process. The r-process is the rapid absorption of high flux neutrons by the nucleus while the s-process is the slow absorption of low flux neutrons by the nucleus. To understand these processes, one could measure the  $(n,\gamma)$ <sup>1</sup> cross sections directly, but these cross sections alone do not inform us much about the nuclear synthesis processes. They do not explain why certain nuclei are produced and why others are not and why they are produced at the proportion and rate that they are produced at.

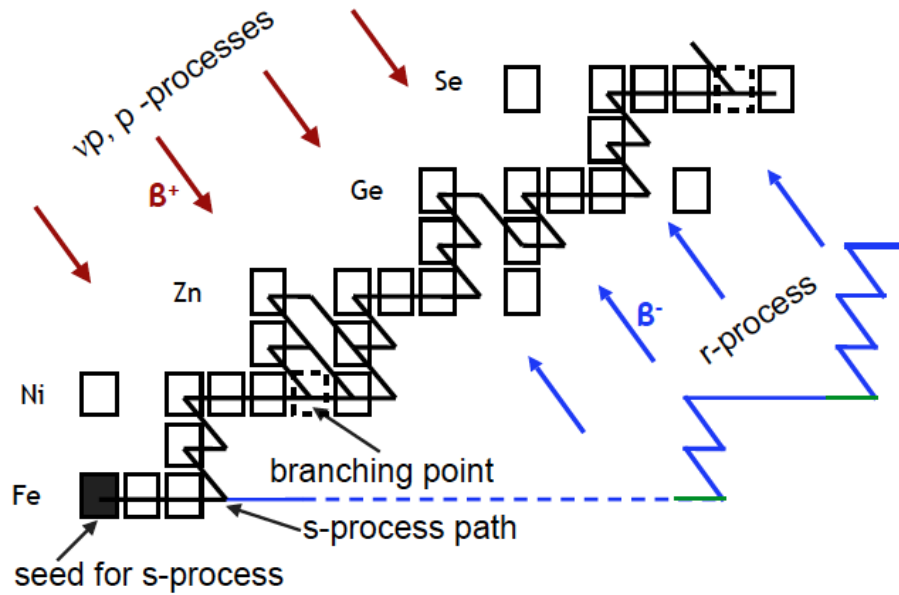


FIGURE 1.3: A schematic representation of the p, r and s-process [8].

Figure 1.3 shows the pathways for p, r and s-processes on the table of isotopes. The black and white boxes represent stable nuclei, the blue arrows region shows neutron-rich nuclei and the brown arrows region shows the proton-rich nuclei. Looking at the s-process, a stable nucleus will absorb a neutron and become unstable. The unstable nucleus will  $\beta^-$  decay to go back to stability, increasing the proton number and thus forming a heavier element. The r-process will see the nucleus absorbing tens of neutrons before  $\beta^-$  decaying to a more stable and heavier element.

There is an interplay between neutron capture and  $\beta$  decay rates which determine the drip line. The s-process takes place in asymptotic giant branch (AGB)

<sup>1</sup> $(n,\gamma)$  absorption cross section is the neutron absorption cross section of a nucleus, in which case after absorbing the neutron it  $\gamma$  decays. The inverse is also possible where the nucleus emits a neutron after absorbing a  $\gamma$ -ray, and is denoted by  $(\gamma,n)$ .

stars [9]. This happens to small and medium sized stars at a late stage of their lives. At the moment there is no clear astrophysical site for the r-process.

To understand more about nucleosynthesis through the r- and s-processes, nuclear level densities (NLD) and the GSF of nuclei can be used. The NLD represents nuclear energy levels per energy range and the GSF describes the ability of nuclei to absorb or emit  $\gamma$  rays at different  $\gamma$  ray energies.

Only  $(n,\gamma)$  cross sections are discussed in this work, but really the GSF describes all nuclear reaction cross sections including  $(p,\gamma)$ ,  $(\alpha,\gamma)$  and other possible reactions that involve the release of a  $\gamma$  ray. The NLD and GSF are two of the input parameters used to calculate  $(n,\gamma)$  cross sections in codes such as TALYS [10].



## 1.2 Motivation

The information provided by  $(n, \gamma)$  cross sections is not only useful in explaining nuclear synthesis in stars [11], but is also helpful in explaining reactions in nuclear reactors [12] and waste transmutation<sup>2</sup> [12].

The GSF is the subject of this thesis work. An increasing number of experiments over the years have revealed the presence of a Low-Energy Enhancement (LEE) [1] in the GSF of elements heavier than iron. This LEE can have a massive implication in the  $(n, \gamma)$  cross sections of heavy nuclei. The impact of the LEE is found to be relatively small on the  $(n, \gamma)$  cross section of stable nuclei [13], which play a minor role in the reaction mechanisms responsible for nuclear synthesis.

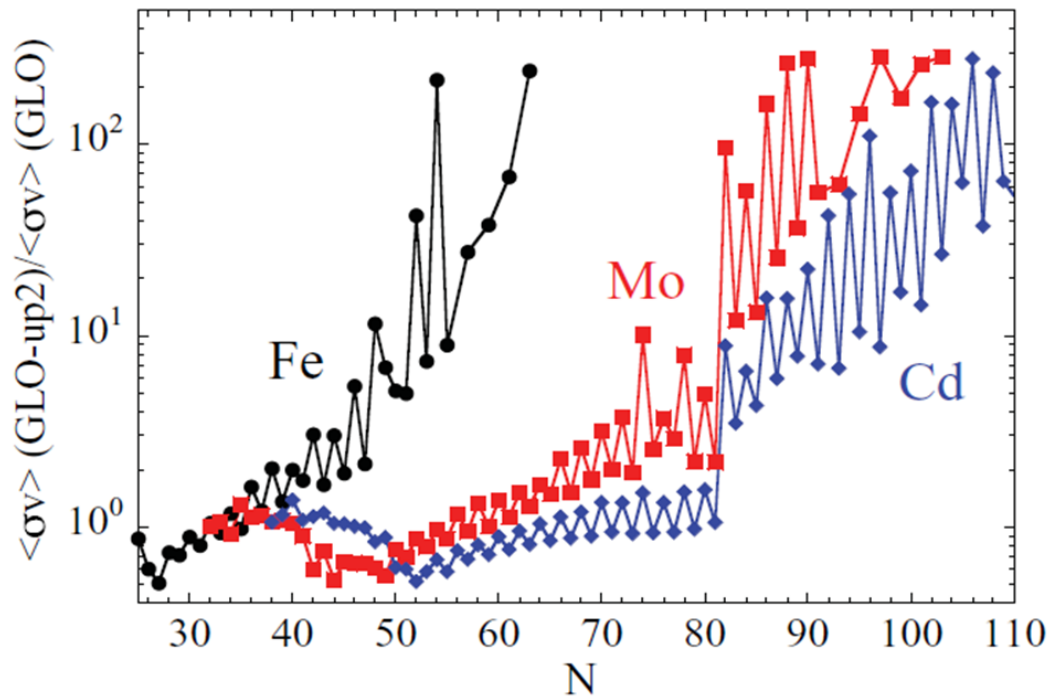


FIGURE 1.4: Ratios of Maxwellian-averaged  $(n, \gamma)$  reaction rates at  $T = 10^9 K$  for the Fe, Mo, and Cd isotopic chains up to the neutron drip line, using the generalized Lorentzian (GLO) model [13].

However, the LEE has a significant effect for exotic neutron-rich nuclei and could potentially increase the nucleosynthesis reaction rates “by one or even two orders of magnitude” [13]. This is due to the fact that the neutron-rich nuclei have low

<sup>2</sup>Conversion of harmful waste from nuclear reactors to less harmful one.



neutron separation energy, which is much closer to the LEE region. The enhancement has a non-negligible impact on the neutron capture rates essential for the r-process nucleosynthesis.

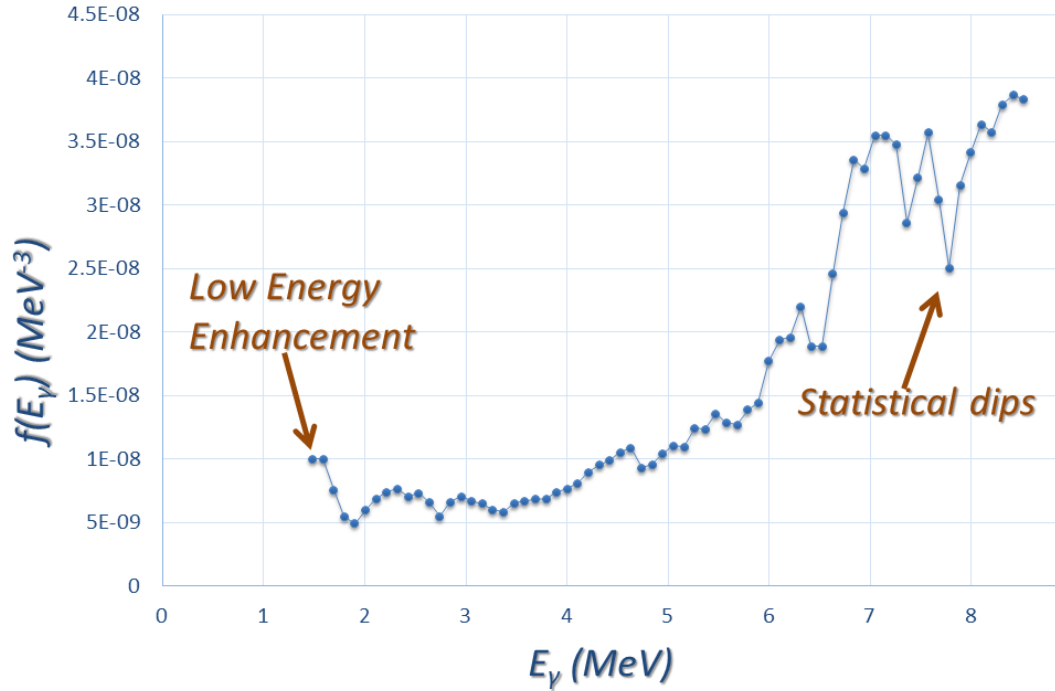


FIGURE 1.5: The  $\gamma$ -ray strength function of  $^{74}\text{Ge}$  from the reaction  $^{74}\text{Ge}(^3\text{He}, ^3\text{He}')^{74}\text{Ge}^*$ , showing the low energy enhancement [3].

Figure 1.5 is a data plot of the GSF of  $^{74}\text{Ge}$  from the reaction  $^{74}\text{Ge}(^3\text{He}, ^3\text{He}')^{74}\text{Ge}^*$  [3]. The experiment was conducted at the Oslo Cyclotron Laboratory (OCL), using singly-ionized  $^3\text{He}$  beams. The beam energy was 38 MeV and the  $^{74}\text{Ge}$  target had a thickness of  $0.5 \text{ mg.cm}^{-2}$ . To analyze the data, the Oslo Method was used, which is a one-step primary  $\gamma$ -ray cascade method. The Oslo Method is fully described in ref. [14] and the LEE was found just below 2 MeV down to 1.5 MeV from the experiment discussed.

The main objective of this project is to measure the GSF of  $^{74}\text{Ge}$  using a different method compared to the one used by Renstrøm [14] and a different reaction. The Ratio Method will be used which involves taking ratios of  $\gamma$ -ray intensities and  $\gamma$ -ray energies from the  $\gamma$ -rays emitted by excited nuclei. The method is model

independent, hence all the parameters used are measured directly in the experiment. The reason for this is to see how the GSF compares when different methods are used to measure the GSF of the same nucleus.

### 1.3 Research Questions

The study of the GSF has come with many open fundamental questions, such as the following:

- Is the shape of GSF at AGB temperature dependent?
- Do different experimental methods yield the same result?
- What is the origin of the LEE?
- Is the Brink-Axel hypothesis [15] valid?

To try and tackle some of these questions, a series of experiments were performed aimed at studying the nucleus  $^{74}\text{Ge}$ . These experiments were performed under different conditions with different projectiles and energies to try and see the relation between the different statistical spectra. Here is the list of the experiments that were conducted:

- $^{74}\text{Ge}(\gamma, \gamma')^{74}\text{Ge}$  was performed at Dresden, Rossendorf, Germany [2].
- $^{74}\text{Ge}(\alpha, \alpha')^{74}\text{Ge}$  was performed at iThemba LABS, South Africa [4].
- $^{74}\text{Ge}(^3\text{He}, ^3\text{He}')^{74}\text{Ge}$  was performed at the University of Oslo, Norway [3].
- $^{74}\text{Ge}(p, p')^{74}\text{Ge}$  was performed at Lawrence Berkeley National Laboratory, United States of America [this work].

## 1.4 Thesis Outline

In this thesis, discussion of the GSF of  $^{74}\text{Ge}$  will be given. The ratio method will be used to carry out the analysis with the goal of investigating the LEE which was previously observed in the reaction  $^{74}\text{Ge}(^3\text{He}, ^3\text{He}')^{74}\text{Ge}^*$  [3]. The ratio method is explained in detail in section 2.6. In chapter 2 a review of the theories of some important concepts is made. Chapter 3 will discuss the experimental setup and techniques used to carry out the experiment and then go in depth about the analysis that is carried out in chapter 4. The last section will be chapter 5 where a discussion and conclusion on the final results will be presented.

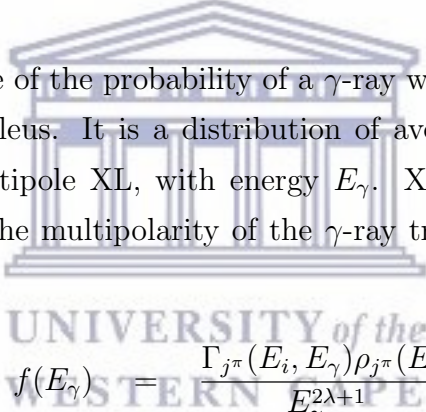


# Chapter 2

## Theory and literature review

### 2.1 $\gamma$ -ray Strength Function

The GSF is a measure of the probability of a  $\gamma$ -ray with energy  $E_\gamma$  to be emitted or absorbed by a nucleus. It is a distribution of average reduced partial width for transitions of multipole XL, with energy  $E_\gamma$ . X is either E (electric) or M (magnetic) and L is the multipolarity of the  $\gamma$ -ray transition. It is given by the formula [16],


$$f(E_\gamma) = \frac{\Gamma_{j^\pi}(E_i, E_\gamma) \rho_{j^\pi}(E_i)}{E_\gamma^{2\lambda+1}} \quad , \quad (2.1)$$

where  $\Gamma_{j^\pi}(E_i, E_\gamma)$  is the average width at the quasi-continuum region with  $j^\pi$  representing the spin and parity from the state in the quasi-continuum region from where the primary  $\gamma$  ray comes from.  $E_i$  is the energy state at the quasi-continuum region and  $E_\gamma$  the primary  $\gamma$ -ray energy.  $\rho_{j^\pi}(E_i)$  is the average level density at the quasi-continuum region and  $E_\gamma^{2\lambda+1}$  is the energy dependence for multipolarity.  $\lambda$  is the multipolarity term with  $\lambda = 0$  being the monopole transition,  $\lambda = 1$  being the dipole mode and so on.

Since it has statistically dependent parameters, the  $\gamma$ -ray strength function is thus an average quantity like the level density. It is a measure of the strength of statistical  $\gamma$ -rays coming from a nucleus excited up to the quasi-continuum region, the region of high level density just below the neutron separation energy.

Figure 2.1 is a schematic representation of a nucleus excited to such a region of excited states. A projectile will excite the nucleus to the quasi-continuum region and the nucleus then de-excites down to the lower discrete states. Since the quasi-continuum region has a very high level density, that is, it has millions of energy level states within 1 MeV energy width, it decays with a lot of  $\gamma$  rays. Hence to measure these  $\gamma$  rays we use statistical measures, which is the GSF.

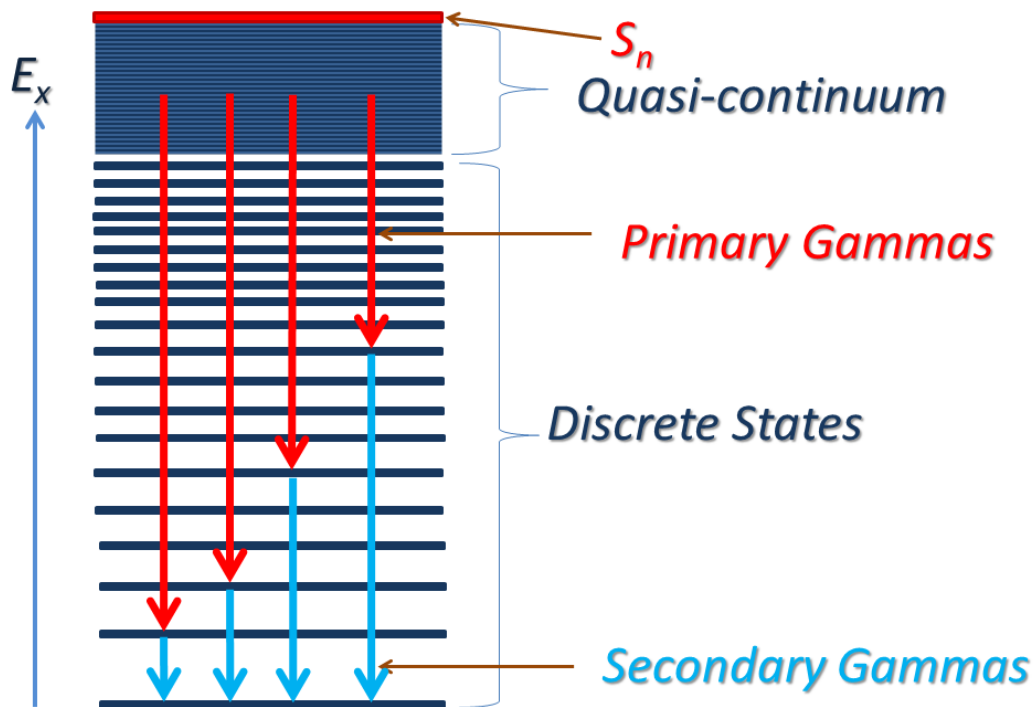


FIGURE 2.1: A schematic of statistical  $\gamma$ -rays originating from the quasi-continuum region.

The GSFs are used as input parameters into model calculations for capture cross sections, especially neutron capture cross sections. They also aid in calculating cross sections for isomeric state populations and used to assess the competition between  $\gamma$ -ray and particle emission. The strength function carries within itself all multipolarity resonances and the giant resonance for all the different multiplicities. The multipolarity measured for a reaction depends on the multipolarity energy term ( $E_\gamma^{2\lambda+1}$ ). For the thesis, dipole resonances ( $E_\gamma^3$ ) where  $\lambda = 1$  were used. This is because the GSF is dominated by dipole transition and there are very few monopole and quadrupole transitions at the energies of study.

## 2.2 Level Density

The nuclear level density (NLD) is an important quantity in nuclear physics, which tells us about nuclear structure at high excitation energies. It is needed for the calculation of cross sections in nuclear reactions. Many nuclear synthesis model calculations require the knowledge of NLD.

In increasing excitation energy, the greater the level density ( $\rho(E_x)$ ) becomes. To obtain the NLD one needs to solve the Schrödinger's equation for the precise potential for all the different states, which can be very tedious to do if even possible at all. To overcome that barrier, statistical models are used to interpret the nuclear states in the region of high level density.

The two statistical models that are going to be discussed on this thesis are the Back-shifted Fermi Gas (BSFG) and the Constant Temperature (CT) models.

### 2.2.1 Back-shifted Fermi Gas model

The nuclear level density has been interpreted using the Fermi gas model for many years over the 20<sup>th</sup> century. Level density formulas introduced by Bethe [17] gained the majority use for statistical model calculations. The problem with Bethe's formulas is that they assume single particle levels to be equally spaced and non-degenerate. The model provides us with only a zeroth-order approximation of a Fermi gas. The original model is characterized by the following level density [18],

$$\rho(E) = \frac{\sqrt{\pi}}{12} \frac{e^{(2\sqrt{aE})}}{a^{1/4} E^{5/4}}, \quad (2.2)$$

where  $E$  is the excited energy of the nucleus and  $a$  is the level density parameter given by [18],

$$a = \frac{\pi}{6} (g_p + g_n), \quad (2.3)$$

where  $g_p$  and  $g_n$  are the single-particle level density parameters for protons and

neutrons, respectively.

A new method was proposed that corrected for the uneven spacing of energy levels and also corrected for odd-even nuclei structure. Again the Fermi gas model was adopted but now with shifted ground state energy and the level density parameter  $a$ , both treated as floating points to be adjusted to the experiment. Reference [19] shows how the floating parameters are adjusted for different nuclei. Here is the nuclear level density formula as presented by Gilbert and Cameron in 1965 [20],

$$\rho(U) = \frac{\sqrt{\pi}}{12} \frac{e^{(2\sqrt{aU})}}{a^{1/4}U^{5/4}} \frac{1}{\sqrt{2\pi\sigma}}, \quad (2.4)$$

where  $U = E - \Delta p - \Delta n$  is the back-shifted energy, with  $E$  being the excited state,  $\Delta p$  and  $\Delta n$  are the proton and neutron pairing energies, respectively. The equation of the total level density (2.4) is derived from the total density of states assuming random coupling of angular momenta. Because of this a new term is introduced, the spin cut-off parameter  $\sigma$ , which describes the spin distribution. The spin cut-off parameter  $\sigma$  is given by [19],

$$\sigma^2 = g \langle m_j^2 \rangle T. \quad (2.5)$$

$\langle m_j^2 \rangle \approx 0.146A^{\frac{2}{3}}$  is the average mean squared projection of the spins and  $T$  is the average nuclear temperature.  $g$  is the density of the single particle states near the Fermi level and is given as [18],

$$g = g_p + g_n, \quad (2.6)$$

and  $T$  is given by [18],

$$T = \sqrt{\frac{U}{a}}. \quad (2.7)$$

## 2.2.2 Constant Temperature model

The Back-shifted Fermi gas model works well for high excitation states, but is inconsistent at low energies. For these low excitation energies between  $0 < Ex < 10$

MeV, the total level densities are better represented by the constant temperature model. The level density formula using the constant temperature model is given as follows [21],

$$\rho(E) = \frac{1}{T} e^{\frac{E-E_o}{T}}, \quad (2.8)$$

where  $E$  is the excitation energy of the nucleus.  $E_o$  is the free parameter for energy shift and  $T$  is the free parameter for constant nuclear temperature. The shift in excitation energy  $E_o$  is determined by [21],

$$E_o = S_n - T \ln[\rho(S_n)T]. \quad (2.9)$$

$S_n$  is the neutron separation energy of the nucleus and  $\rho(S_n)$  is the level density at the neutron separation energy.

## 2.3 $\gamma$ -ray Cascade from Quasi-continuum

The purpose of the project is to excite the  $^{74}\text{Ge}$  nucleus into the region between the discrete states and the neutron separation energy, called the quasi-continuum region. The quasi-continuum region is vital in understanding the NLD and GSF as it has nuclear statistical properties. To make measurements of GSFs for the  $^{74}\text{Ge}$  nucleus, particle- $\gamma$ - $\gamma$  coincidences must be extracted.

Figure 2.2 is a schematic diagram showing how these coincidences are made. A full cascade of  $\gamma$  rays is made up of two  $\gamma$  rays, one from the quasi-continuum and the other from the discrete states. A gate is applied on an energy region at the quasi-continuum level such that only two  $\gamma$  rays come out. The two  $\gamma$  rays added together must add up to the gated excited state, meaning that the primary  $\gamma$  ray plus the secondary  $\gamma$  ray from the well known excited states form the cascade. If they do not add up to the gated excited state, then the event is rejected, as shown on the right on figure 2.2. More details about how this gate is carried out is given in chapter 4, in section 4.4. Each event is made up of a cascade and all of them together form a nuclear response pattern. The pattern is known as nuclear resonances.



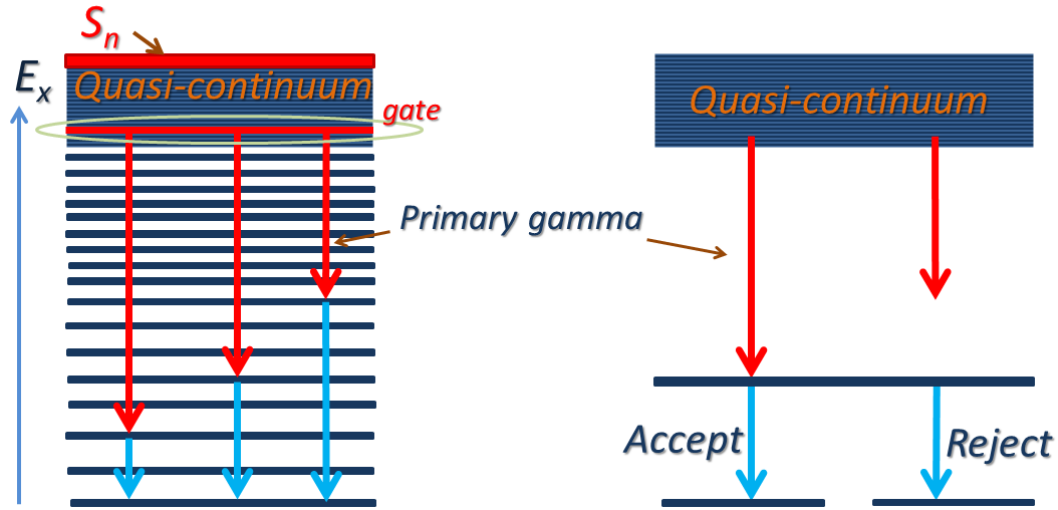


FIGURE 2.2: A schematic representation of the  $\gamma$ -ray cascade method used to construct the strength functions.

## 2.4 The Giant Dipole Resonance (GDR)

Baldwin and Kleiber made the first observation of the Giant Dipole Resonance (GDR) in 1947 through photo-absorption and photo-fission experiments. They observed an increase in the absorption cross section above 10 MeV in a number of nuclei with resonance energies from  $E_x$  16 MeV to 30 MeV. Goldhaber and Teller interpreted the observed broad structure in the  $\gamma$ -absorption spectrum as the excitation of a collective nuclear vibration in which all the protons in the nucleus move collectively against all the neutrons in separate, rigid spheres, creating an electric dipole moment.

Since then, a lot of studies have been made on the GDR and a wide range of systematics for almost all stable nuclei exists on the GDR built on the ground state. Most of the information gathered was extracted from photo-absorption experiments because of the high selectivity of this reaction to E1 transitions. The shape of the resonance in the photo-absorption spectrum can be approximated, in the case of a spherical nucleus, by a single Lorentzian distribution as follows [22],

$$\sigma(E_\gamma) = \frac{\sigma_o E_\gamma^2 \Gamma_{GDR}^2}{(E_\gamma^2 - E_{GDR}^2)^2 + E_\gamma^2 \Gamma_{GDR}^2}, \quad (2.10)$$

where  $E_\gamma$  is the  $\gamma$ -ray energy absorbed by the nucleus,  $\sigma_o$  the strength of each  $\gamma$ -ray

transition,  $E_{GDR}$  the centroid energy and  $\Gamma_{GDR}$  the width of the resonance. Even though this gives a good explanation of the GDR, it is still a model. When the nucleus is statically deformed, the GDR splits into two parts corresponding to oscillations along and perpendicular to the symmetry axis and the photo-absorption cross section can be well reproduced by the superposition of two Lorentzian distributions. This feature allows us to extract the nuclear deformation from the centroid energies of the two components and to distinguish, from the relative intensities, prolate from oblate deformations.

The shell structure affects the width of the resonance with values ranging from 4-5 MeV for closed shell nuclei. This is equivalent to the neutron separation energy of  $^{84}\text{As}$  which is 4.256 MeV, to put the value into perspective. The collectiveness of excited states, relating to the number of participating nucleons, can be estimated in terms of the Energy Weighted Sum Rule (EWSR) for dipole radiation. This rule gives the total integrated cross section for electric dipole photon absorption and is given by [22],

$$\int_{min}^{max} \rho(E_\gamma) dE_\gamma = \frac{2\pi^2 e^2 \hbar}{Mc} \frac{NZ}{A}, \quad (2.11)$$

where  $N$  is the neutron number and  $Z$  the proton number,  $A$  the mass number,  $M$  the nucleon mass and  $c$  the speed of light. Figure 2.3 is a schematic representation of the GDR of a spherical nucleus.

One can visualise the GDR as a high-frequency, damped, almost harmonic vibration around the equilibrium density of the nucleus. The amplitude of the vibration is small compared to the nuclear radius. The restoring forces for these resonances are directly related to macroscopic properties of the nucleus and they provide us with the most reliable information on the bulk properties of the nucleus such as multipolarity.

The GDR is a macroscopic property as it shows the statistical properties of the nucleus, as opposed to microscopic properties which focus on individual excitations of protons and neutrons into different nuclear states. There are two types of collective vibrational modes of nucleons, namely the isoscalar and isovector modes.

These modes are classified according to their multipolarity  $L$ , spin  $S$  and isospin  $T$

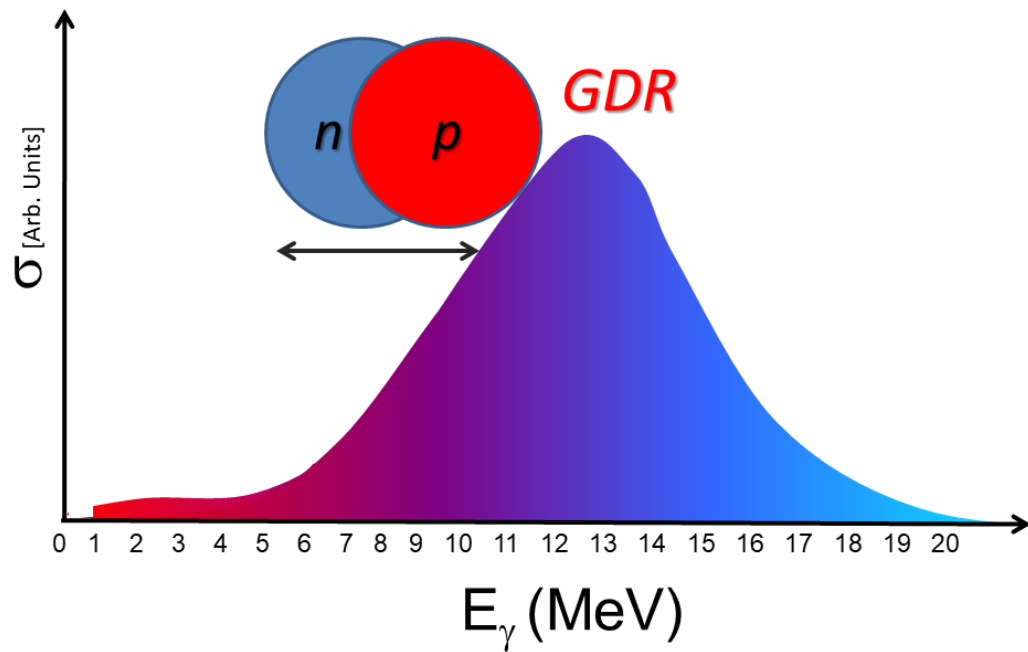


FIGURE 2.3: The Giant Dipole Resonance.

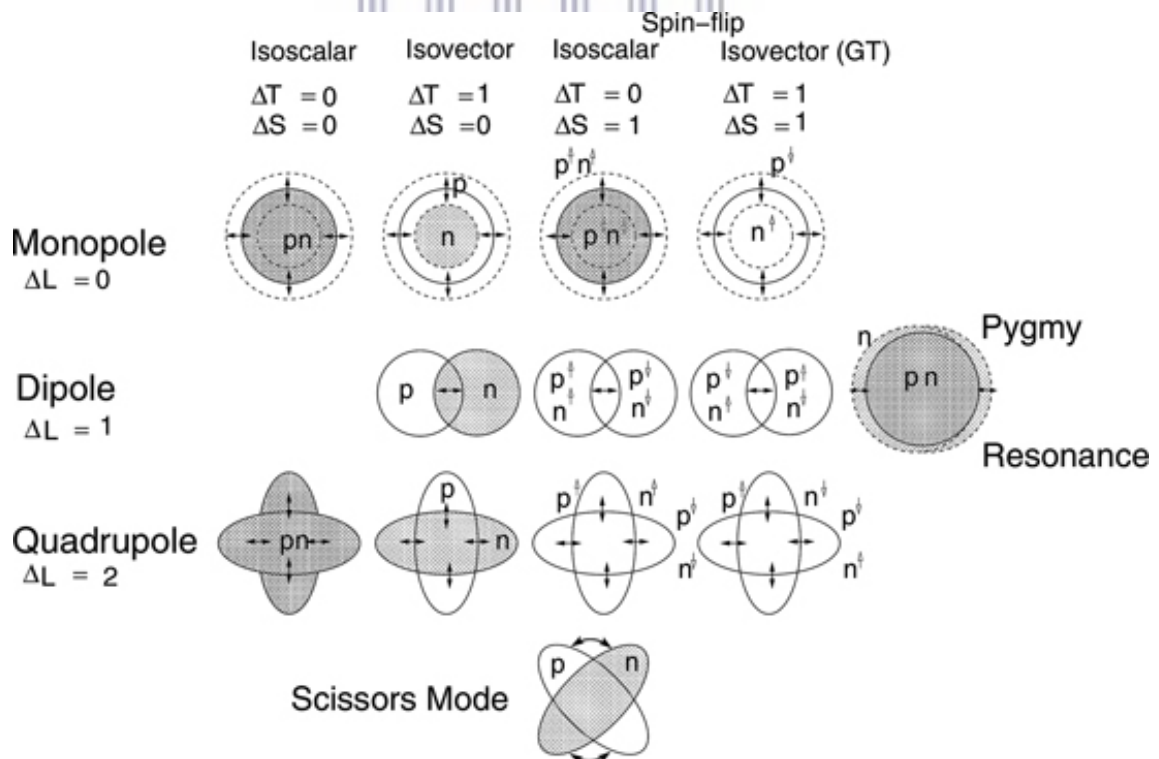
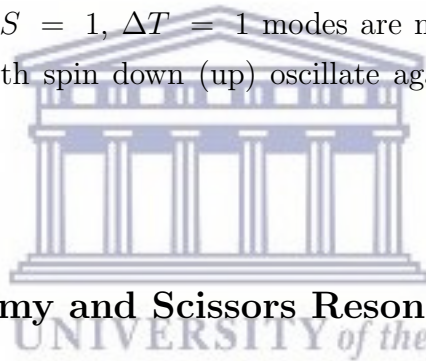


FIGURE 2.4: A qualitative scheme of giant resonance modes of the nucleus, courtesy of [12].

quantum numbers. The  $\Delta S = 0, \Delta T = 0$  modes are electric, isoscalar vibrations in which the protons and neutrons oscillate in phase according to a multipole pattern defined by  $\Delta L = 0, 2, \dots$ . For the electric resonance, the  $\Delta L = 1$  vibration is missing. To first order, it corresponds to a translational motion of the nucleus as a whole and is thus not an intrinsic nuclear excitation.

The  $\Delta S = 0, \Delta T = 1$  modes are electric, isovector vibrations in which the protons and neutrons oscillate out of phase against each other according to a multipole pattern defined by  $\Delta L$ . For the same multipole mode the isovector ones will be at a higher excitation energy than the isoscalar ones since extra energy is required to separate the neutron and proton distributions.

The  $\Delta S = 1, \Delta T = 0$  modes are magnetic, isoscalar vibrations in which nucleons with spin up vibrate against nucleons with spin down, again in a multipole pattern given by  $\Delta L$ . The  $\Delta S = 1, \Delta T = 1$  modes are magnetic, isovector modes in which the protons with spin down (up) oscillate against neutrons with spin up (down).



### 2.4.1 The Pygmy and Scissors Resonances

The GDR is not the only possible resonance model to describe  $\gamma$ -ray absorption cross sections. There are also lower energy resonance models such as the Pygmy and Scissors resonances. Figure 2.5 is a schematic diagram showing these two additional resonance models.

In the Pygmy resonance model there is a stable proton-neutron core and an excessive neutron skin, and these two move against each other. In the Scissors resonance the protons and the neutrons move against each other like a pair of scissors. These resonances are found in deformed, neutron rich nuclei, near the particle emission threshold.

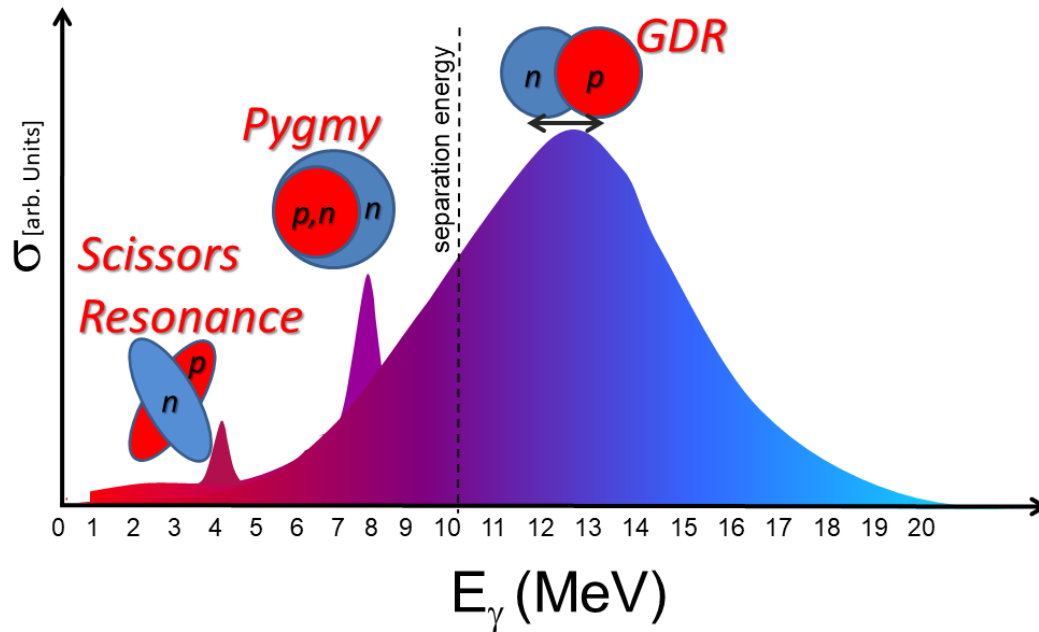


FIGURE 2.5: The schematic of the Giant Dipole Resonance with the Pygmy and Scissors resonances.

## 2.5 $\gamma$ -ray Strength Function and Cross sections

Interactions between neutrons and matter can be one of two, scattering or absorption. Scattering results in change in energy and direction of motion and absorption results in complete absorption of the nucleus by a medium. Both interactions will leave the nucleus in an excited state. The nucleus will decay by any of the following processes: fission reaction where the nucleus splits apart into two large fragments, alpha particle emission or by the emission of a  $\gamma$  ray. The first three modes of decay may also be accompanied by an emission of a  $\gamma$  ray.

Another important reaction that requires the knowledge of the GSF is the neutron capture reaction. When a nucleus captures a neutron, it transitions to an excited isotope. To de-excite from this state, it emits  $\gamma$  rays. These kind of reactions,  $(n, \gamma)$  reactions, are important in nuclear astrophysics in the formation of heavy nuclei during a supernova explosion.

The GSF together with the level density are used to calculate the transmission

coefficient ( $T$ ), which is applied into TALYS<sup>1</sup> software to calculate (n, $\gamma$ ) cross sections. The transmission coefficient is of the form [18],

$$T_{XL}(E_\gamma) = 2\pi E_\gamma^{2\lambda+1} f_{XL}(E_\gamma), \quad (2.12)$$

where  $E_\gamma^{2\lambda+1}$  is the  $\gamma$  ray dependence factor,  $f_{XL}(E_\gamma)$  the GSF and the factor  $2\pi$  is a scaling factor for the total cross section of transmitting a  $\gamma$  ray.  $XL$  is the multipolarity of the electromagnetic wave that is transmitted.

## 2.6 The Ratio Method

This method involves the taking of ratios of relative GSF. As shown in figure 1.5, the GSF for statistical  $\gamma$ -ray transitions is given by [16],

$$f(E_\gamma) = \frac{\Gamma_{j\pi}(E_i, E_\gamma) \rho_{j\pi}(E_i)}{E_\gamma^{2\lambda+1}}. \quad (2.13)$$

The intensity of primary transitions  $N_L$ , where  $L$  are the energy levels to which the primary  $\gamma$  rays decay to, is directly proportional to the average width from energy  $E_i$ , average level density and cross section of  $\gamma$  rays being emitted from  $E_i$  [1],

$$N_L \propto \Gamma_{j\pi}(E_i, E_\gamma) \rho_{j\pi}(E_i) \sigma_{j\pi}(E_i). \quad (2.14)$$

The quantity  $\sigma_{j\pi}(E_i)$  is the cross section for populating the levels with given spin and parity at excitation energy  $E_i$ . So if we use information from equation 2.12, the  $N_L$  is [1],

$$N_L = f(E_\gamma) E_\gamma^{2\lambda+1} \sigma_{j\pi}(E_i). \quad (2.15)$$

If the  $\gamma$ -rays all go to the same spin state, then  $\sigma_{j\pi}(E_i)$  does not change considerably. That is because  $\sigma_{j\pi}(E_i)$  depends on spin and parity, which stay the same

<sup>1</sup>A code used to calculate many nuclear cross sections including (n, $\gamma$ ) cross sections. <http://www.talys.eu>

because states with the same spin and parity are grouped together. Therefore if the primary  $\gamma$  rays go to the same spin states, the cross sections will cancel out when taking the ratios of the GSF, giving,

$$\frac{f(E_1)}{f(E_2)} = \frac{N_{L_1} E_2^{2\lambda+1}}{N_{L_2} E_1^{2\lambda+1}}, \quad (2.16)$$

where  $N_{L_1}$  and  $N_{L_2}$  are the  $\gamma$  ray intensities for the first and second primary  $\gamma$  rays, respectively.  $E_1^{2\lambda+1}$  is the  $\gamma$  ray energy of the first primary  $\gamma$  ray and  $E_2^{2\lambda+1}$  is the  $\gamma$  ray energy for the second primary  $\gamma$  ray. Thus the ratios only require primary  $\gamma$  ray intensities and energies of the primary  $\gamma$  rays.

Figure 2.6 is a schematic representation of how the branching and the ratios are extracted. The different portions on the banana spectra correspond to different excited states as shown on the picture in the middle. The  $\gamma$  rays that are considered on the far right image are those that correlate to the gated states and form a cascade down to the ground state. Those that do not form a cascade are dismissed.

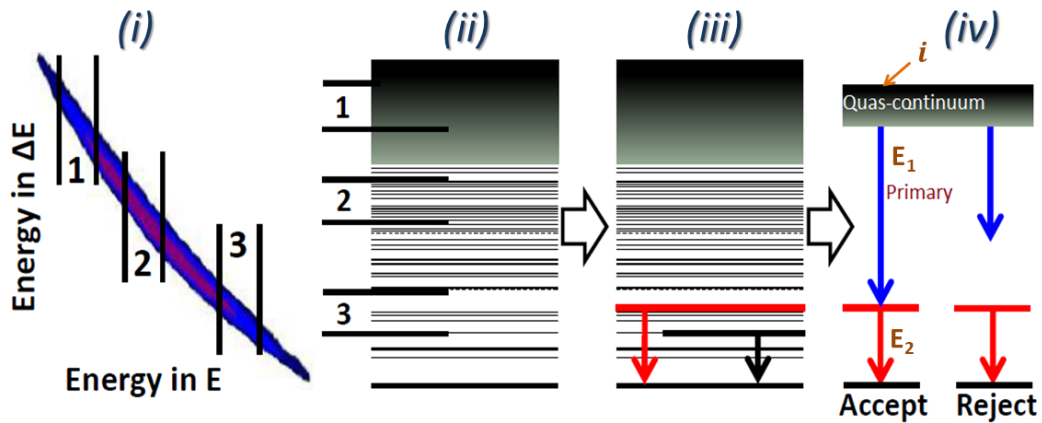


FIGURE 2.6: A schematic representation of how the primary  $\gamma$  rays are extracted for the ratios. (i) Gates are applied to different excited states on the proton spectra. (ii) How the gates apply to the energy level scheme of the  $^{74}\text{Ge}$  nucleus. (iii) After the proton gate, a  $\gamma$  ray gate is applied to a well known low lying state. (iv) A primary  $\gamma$  ray is required such that when one adds it up to the lower lying  $\gamma$  ray, they add-up to the total excitation energy defined by the proton gate.

Partial strength function ratios are taken for the  $\gamma$  rays that are labeled blue in



the figure, i.e., primary<sup>2</sup>  $\gamma$  rays that come from the quasi-continuum region. We assume that dipole transitions dominate, since we make measurements in the region  $E_x = 3$  to 10 MeV, which is largely dominated by the GDR which is of  $E1$  nature. Then equation 2.16 becomes

$$\frac{f(E_1)}{f(E_2)} = \frac{N_{L_1} E_2^3}{N_{L_2} E_1^3}. \quad (2.17)$$

We already have the intensity of primary transitions  $N_{L_n}$  and the primary  $\gamma$ -ray energies  $E_n$ <sup>3</sup>, where subscript  $n$  is an index referring to the  $\gamma$  ray, from the particle- $\gamma$ - $\gamma$  coincidence events.




---

<sup>2</sup> $\gamma$ -rays that come directly out of the quasi-continuum region.



# Chapter 3

## Experimental Techniques

### 3.1 Details of the experiment

The data were collected with the STARS-LiBerACE [23] array at the Lawrence Berkeley National Laboratory, California. The STARS stands for Silicon Telescope Array for Reaction Studies and LiBerACE stands for Livermore Berkeley Array for Collaborative Experiments. The latter is an array of six Compton-suppressed high-purity germanium clover detectors for good energy resolution detection of  $\gamma$  rays. It is complemented by the silicon detector telescope to specify entrance excitation energies of the charged particles.

A proton beam with energy of 18 MeV bombarded a  $^{74}\text{Ge}$  target with thickness of  $0.5 \text{ mg/cm}^2$ , populating states through the reaction  $^{74}\text{Ge}(p,p')^{74}\text{Ge}^*$ . There were other channel reactions visible though, like the  $^{74}\text{Ge}(p,d)^{73}\text{Ge}^*$  channel, but they are removed by placing a gate on proton ejectiles. The beam current was about 7 pA on average. The experiment was carried out for five days.

### 3.2 High Purity Germanium Detectors

For  $\gamma$ -ray detection, the LiBerACE array of six Compton-suppressed high purity germanium (HPGe) detectors was used, with the sixth one not functional and hence was omitted. Each of the four n-type germanium crystals has a diameter of

50 mm and a length of 80 mm, and they are arranged as a four-leaf clover inside a common cryostat. N-type semiconductors have a larger electron concentration than hole concentration and the term n-type itself comes from the negative charge of the electron. In n-type semiconductors, electrons are the majority carriers and holes, which are positive vacancies as a result of the absence of electrons, are the minority carriers.

N-type semiconductors are created by doping an intrinsic semiconductor with donor impurities and a common dopant for n-type silicon is phosphorus. In an n-type semiconductor, the Fermi level is greater than that of the intrinsic semiconductor and lies closer to the conduction band than the valence band.

Each clover is surrounded by 16 optically-isolated SCIONIX Bismuth Germanate Oxide (BGO) Scintillators [23] that are operated as a Compton-suppression shield.

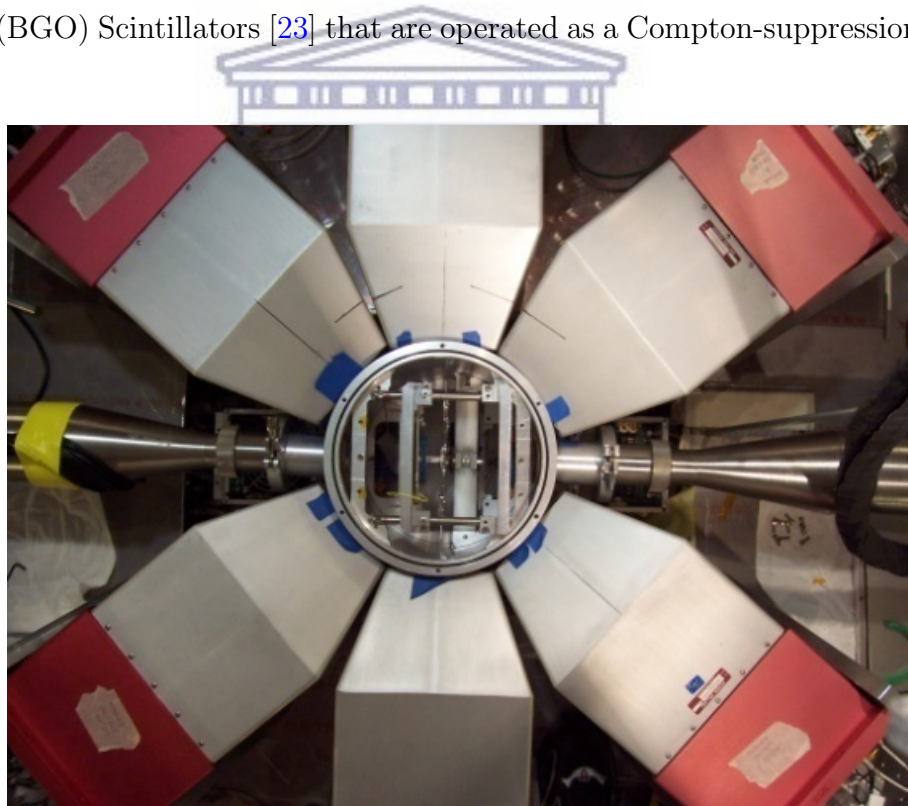


FIGURE 3.1: The clover detectors used for  $\gamma$ -ray detection [24].

The purpose of using HPGe detectors is to convert  $\gamma$  rays into electrical signals which can be used to determine both the energy and the intensity of the  $\gamma$  rays detected. The semiconductor operating principle is ionization, and the passage of ionizing radiation creates electron hole pairs which are separated and collected on

anode/cathode using an electric field. They are crystalline materials whose outer shell atomic levels show an energy band structure with a valence band, a forbidden energy gap and a conduction band. Figure 3.3 shows the structure of metallic, semiconductor and insulating materials.

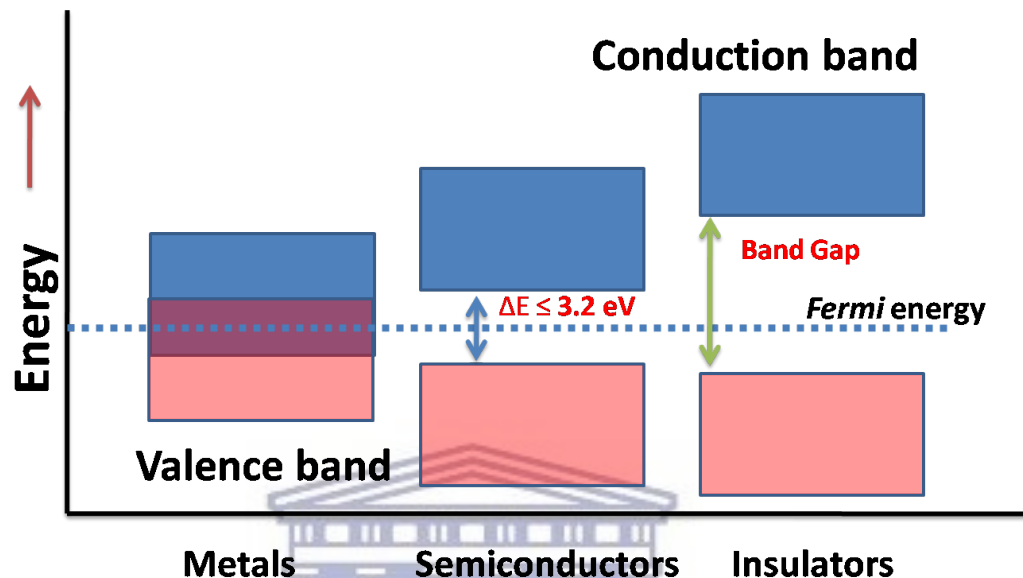


FIGURE 3.2: Energy band gap schematic showing the structure of metals, semiconductors and insulators [25].

The valence and conduction bands are energy levels of the atom which arise as a result of the periodic arrangement of the atoms in the crystal, while the forbidden energy gap is a region with no available energy levels at all. The highest-energy band is the conduction band and electrons in this region are free to roam about the entire crystal.

The electrons in the valence band levels, on the other hand, are more tightly bound and remain associated to their respective atom. The width of the gap and bands is determined by the lattice spacing between the atoms which is dependent on the temperature and the pressure on the lattice structure. The electric current in a semiconductor arises as a consequence of movement of free electrons in the conduction band and the movement of holes in the valence band. The signal is amplified and shaped, then recorded using a data acquisition system where the information of the signal received is recorded for further processing.

### 3.3 Silicon Detector Telescope (SDT)

For particle detection, two *S2* 64 channel silicon detectors [26] were used. The *S2* silicon detector has 48 rings and 16 sectors. The two *S2* detectors had two different thicknesses, the thinnest detector was used as a  $\Delta E$  and the thicker detector was used as E. The  $\Delta E$  silicon detector was about 140  $\mu\text{m}$  thick while the E silicon was about 1000  $\mu\text{m}$  thick.

The SDT had an angular range from  $49^\circ$ - $75^\circ$  with respect to the beam axis. Facing the target was the ring side of the  $\Delta E$  silicon detector, with its sectors facing that of the E telescope. The distance between the *S2* and the target was 19 mm, and the distance between the  $\Delta E$  and E telescope was 2.4 mm. The telescope was placed in such a way that the sectors were back to back. So the  $\Delta E$  rings were facing the beam while the E rings were facing away from the beam direction.

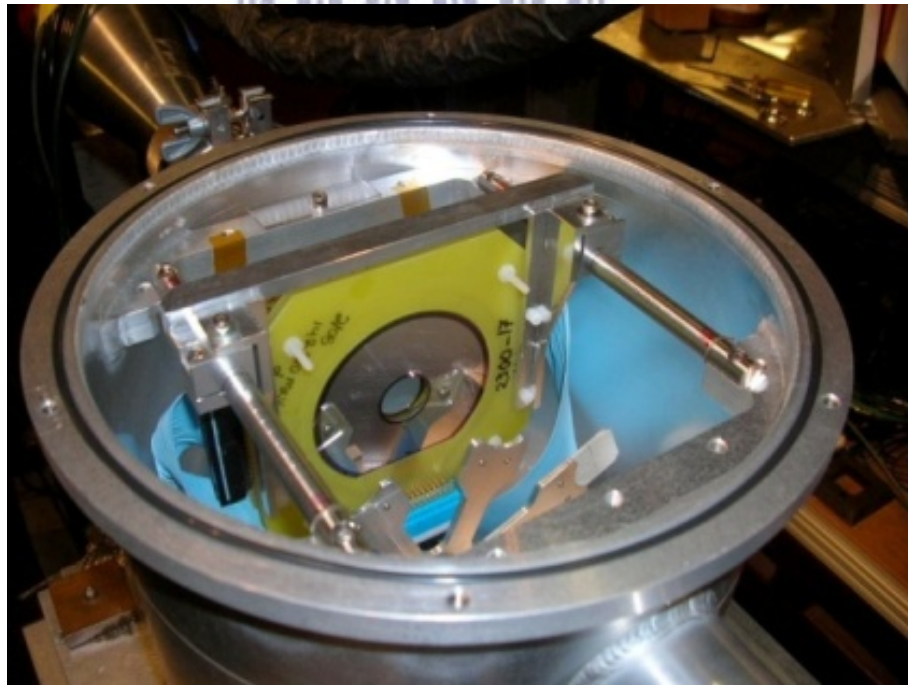


FIGURE 3.3: The Silicon Detector Telescope (SDT) used for proton detection [24].

Figure 3.3 shows a picture of the SDT mounted in the scattering chamber. The cylindrical scattering chamber that holds STARS has a height of 24 cm and a diameter of 25 cm. The chamber is made out of aluminum with a wall thickness of 0.4 cm to limit the attenuation of  $\gamma$  rays emerging from the target.

A  $12.5\ \mu\text{m}$  thick aluminum foil was placed in front of the silicon telescopes to shield them from delta electrons, very fast electrons knocked out of atomic orbit by energetic charged particles, that are produced by the proton beam hitting the target frame and other metals. Silicon detectors use the same working principles as the germanium detectors in that they are both semiconductors. It is different from the germanium detector in that it has a bigger band gap which makes it better suited for charged particle detection. Its advantage is that it operates well at room temperature and thus does not have to be attached to a cooling system.

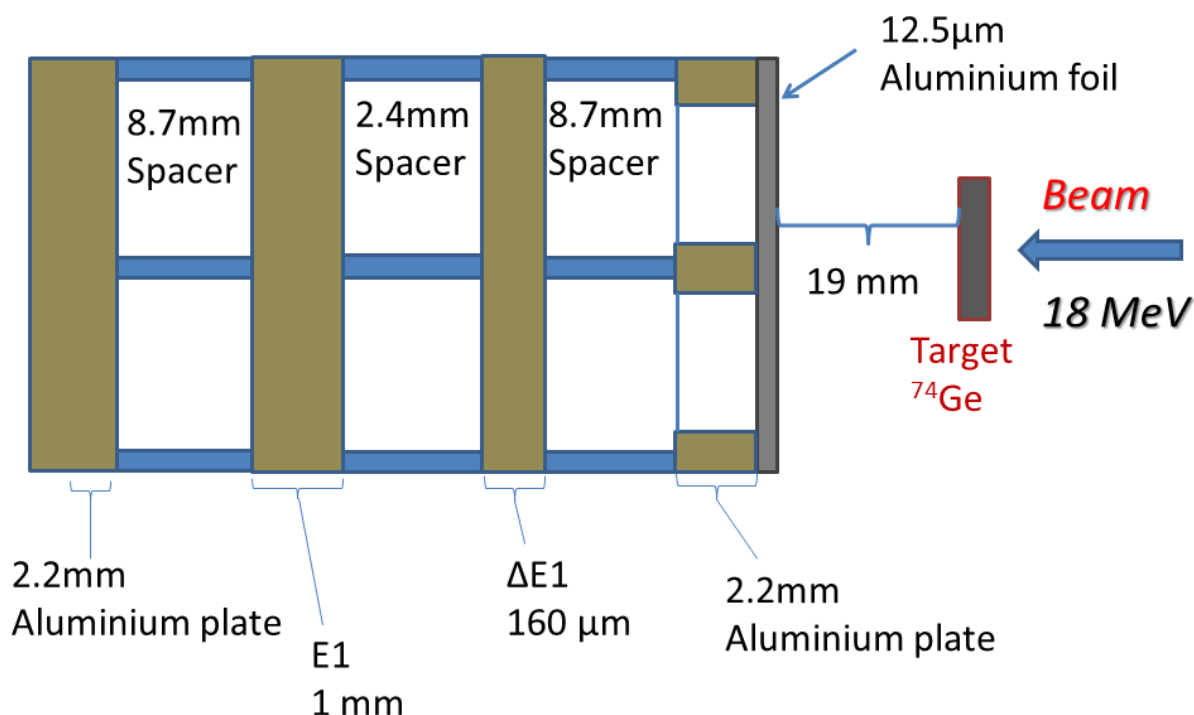


FIGURE 3.4: A schematic representation of the silicon setup.

A reverse-bias voltage was applied to the telescope with 45 V on the front  $\Delta E$  detector at a leakage current of  $7.3\ \mu\text{A}$  and 135V on the back E detector at a leakage current of  $9.3\ \mu\text{A}$ . The signals detected by the silicon detector telescope first goes through the analogue electronics to be amplified and shaped, and then sent to the data acquisition system where the signal is interpreted in terms of energy and time.

### 3.4 Signal Processing

The  $\Delta E$  silicon had the 24 rings positively biased to 45 Volts while all the 16 sectors were grounded and the E silicon had its 24 rings positively biased to 135 Volts. Bias voltage was applied through a resistor network which passively limits the current. Connection from the SDT to the bias voltage was established through custom breakout boards which were located inside the vacuum chamber. The signals are transferred from the chamber to the air side of the chamber through custom NEMA-G [23] vacuum feedthroughs.

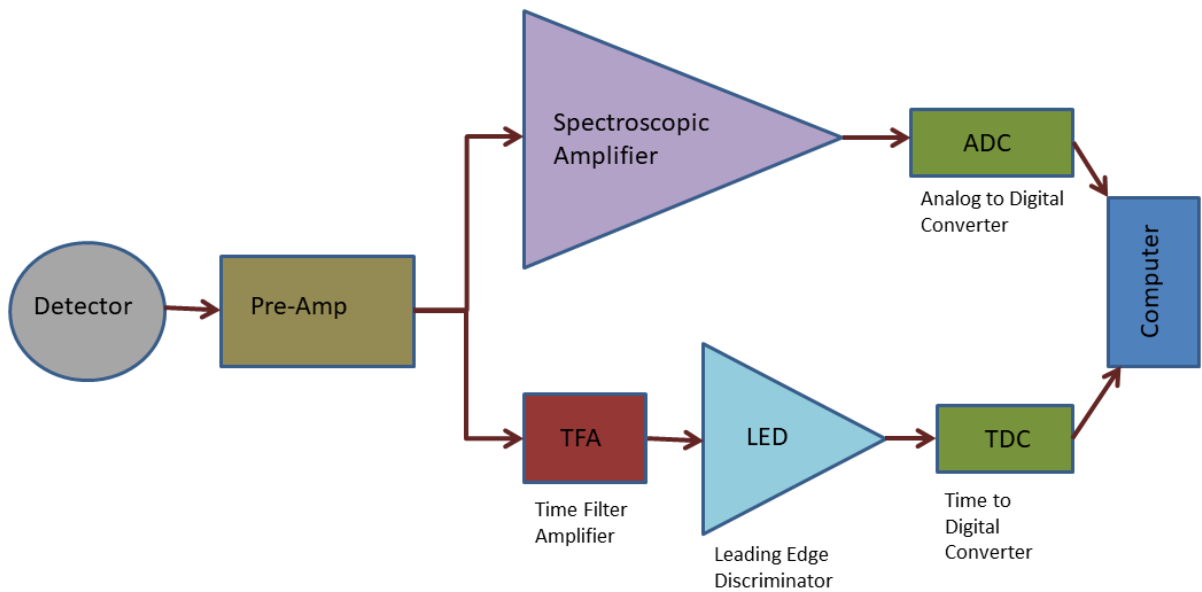


FIGURE 3.5: A schematic representation of analogue electronics setup.

The SDT signals are amplified using Charge8V [23] charge-sensitive pre-amplifiers from Swan Research. The pre-amplifier plugs into a Printed Circuit Board (PCB) [23] motherboard that provides power and the ability to test the pre-amplifier response with a pulser signal. Each motherboard has 16 pre-amplifiers and is located next to the vacuum feedthrough on each side of the chamber. The motherboards are shielded from electrical conductivity with each other by an aluminum box and the amplifiers are cooled down by a fan. The total length from the detectors to the pre-amplifiers is less than 60 cm.

The pre-amplifier output is further amplified and shaped by CAEN N568B shapers



[23] which have 1 k $\Omega$  input impedance. Each of the eight shapers provide 16 fast and 16 slow outputs. The fast signals are discriminated using Leading-Edge Discriminators (LED). For the  $\Delta E$ -E telescope configuration, the discriminated  $\Delta E$  (E) output signals are joined together and stretched to a 100 ns (400 ns) logic signal. The particle trigger is formed from the overlap of these two signals.

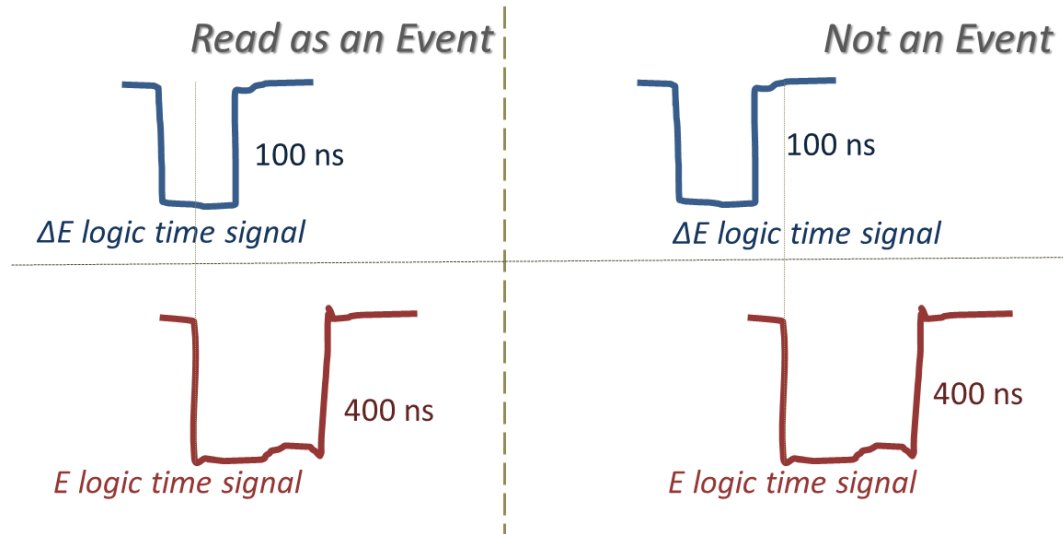


FIGURE 3.6: A schematic representation of time gates on the Silicon Detector Telescope. So the time logic signals constitute a single event since the second signal comes within a space of less than 100 ns after the first one, while the second is not an event since the second signal comes after the required 100 ns gap.

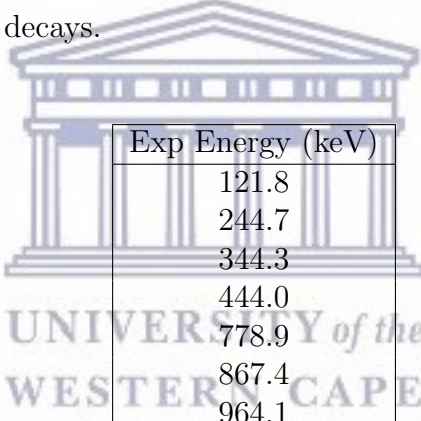
Figure 3.6 shows how charged particle events are created using time coincidences. Once the signal comes out of the LED, it feeds into the Time-to-Digital Converter (TDC). The  $\Delta E$  time logic signal is read first, and the E time logic signal has to be registered within 100 ns of the  $\Delta E$  signal for the two time signals to be registered as an event. This constitutes a particle single event. The TDC start signal were the  $\gamma$ -rays and the stop were charged particles.

For the Compton-suppressed clover detectors, there was a single custom-built CAMAC-based module used to process the signals. Each of the CAMAC-based modules combines four high-resolution shaping amplifiers, TFA, and constant fraction discriminators (CFD), three side-channel amplifiers, an 8-channel BGO processor with eight fast timing amplifiers, a 14-bit Analog to Digital Converter (ADC), and Compton-suppression logic.

For particle- $\gamma$  coincidences, a logic particle gate was set on the  $\Delta E$  at 50 ns and was 100 ns for the germanium detectors. A coincidence event was established in the same manner as was done for the SDT events, requiring that the germanium logic signal comes within 50 ns after the  $\Delta E$  signal is registered. Particle- $\gamma$ - $\gamma$  gates were also set, requiring that the two  $\gamma$  ray signals come within the first 50 ns of the  $\Delta$  silicon detector firing. The back E silicon detector also had a time gate of 50 ns.

### 3.5 Calibration of data

Before any work can be done on any collected data, an energy calibration has to be performed. Table 3.1 shows the energy transitions obtained from the decay of  $^{152}\text{Eu}$ , which was used for the  $\gamma$  ray calibration. The last transition belongs to  $^{208}\text{Pb}$  after  $^{208}\text{Tl}$  beta decays.



Exp Energy (keV)
121.8
244.7
344.3
444.0
778.9
867.4
964.1
1085.8
1112.1
1408.0
2614.5

TABLE 3.1: The table shows the experimental data of  $\gamma$ -ray energies retrieved from National Nuclear Data Center (NNDC) website [27], which were used to calibrate the data.

To calibrate the HPGe detector,  $^{152}\text{Eu}$  was used as a  $\gamma$ -ray source. It disintegrates 72.1 % by electron-capture, about 0.027 % by  $\beta^-$  to  $^{152}\text{Sm}$  and 27.9 % by  $\beta^+$  emission to  $^{152}\text{Gd}$ . The results on table 3.1 were used to make the energy calibrations. The channel values and the experimental values from NNDC were inputted into the software ecal, and the software made the energy corrections using a linear fit. The table just shows two  $\gamma$  ray data sets out of 20 that were used.



Entry	Channel	Exp Energy	Entry	Channel	Exp Energy
1	982.0	4784.34	1	976.0	4784.34
2	1128.6	5489.48	2	1121.6	5489.48
3	1235.4	6002.35	3	1226.9	6002.35
4	1585.5	7686.80	4	1572.6	7686.80

TABLE 3.2: The table of proton energy calibration.  $^{226}\text{Ra}$  alpha source was used for the calibration, where the second column shows the channel values and the third column shows the corresponding energy values taken from NNDC [27].

$^{226}\text{Ra}$  was used as an  $\alpha$  radiation source to calibrate the Silicon Detector Telescope. The nucleus  $^{226}\text{Ra}$  has a half life of 1600 years before alpha decaying to  $^{222}\text{Rn}$  which has a half life of 3.8 days. The nucleus  $^{222}\text{Rn}$  alpha decays to  $^{218}\text{Po}$  which  $\alpha$  decays to  $^{214}\text{Pb}$  or  $\beta$  decays to  $^{218}\text{At}$ . The nucleus  $^{214}\text{Pb}$   $\beta$ -minus decays to  $^{214}\text{Bi}$  which has 99.979% chance of  $\beta$  decaying to  $^{214}\text{Po}$  and 0.021% of  $\alpha$  decaying to  $^{210}\text{Tl}$ . The nucleus  $^{210}\text{Tl}$  will  $\beta$  decay to  $^{210}\text{Pb}$ .

The nucleus  $^{218}\text{At}$  has 99.9% chance of  $\alpha$  decaying to  $^{214}\text{Bi}$  and 0.1% chance of  $\beta$  decaying to  $^{218}\text{Rn}$ . The nucleus  $^{218}\text{Rn}$  will  $\alpha$  decay to  $^{214}\text{Po}$  which also  $\alpha$  decays to  $^{210}\text{Pb}$ . The decay chain for  $^{226}\text{Ra}$  is shown in figure 3.9. A total of 64 channels were calibrated for the silicon detector telescope, and each channel was functional.

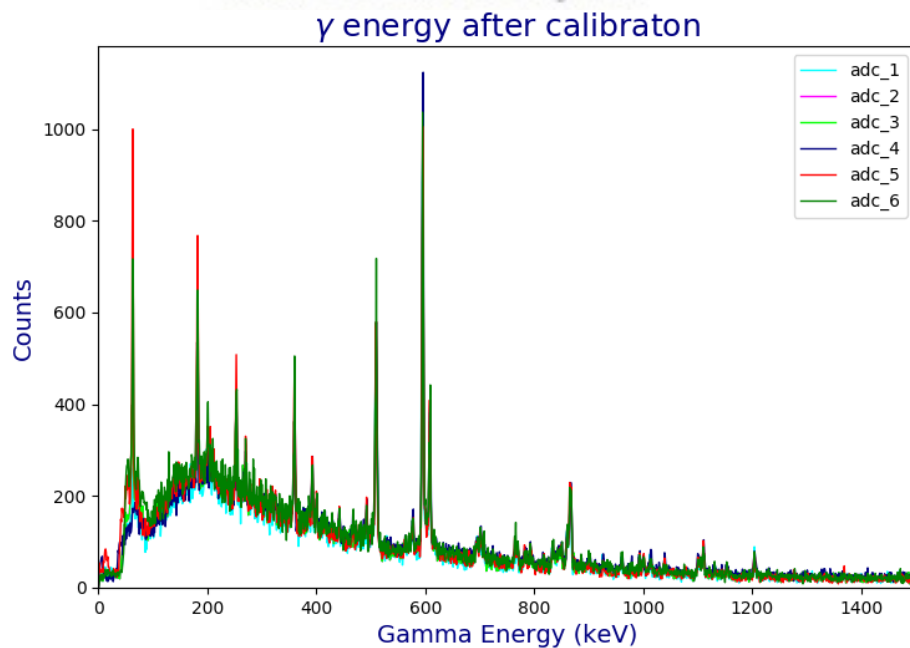


FIGURE 3.7: The six spectra from  $^{74}\text{Ge}$  after calibration was performed. All the energy peaks are correctly overlaid on top of each other.

Figure 3.7 shows the  $\gamma$ -ray spectra of  $^{74}\text{Ge}$  after energy calibration is performed. All of the peaks can be used for analysis.

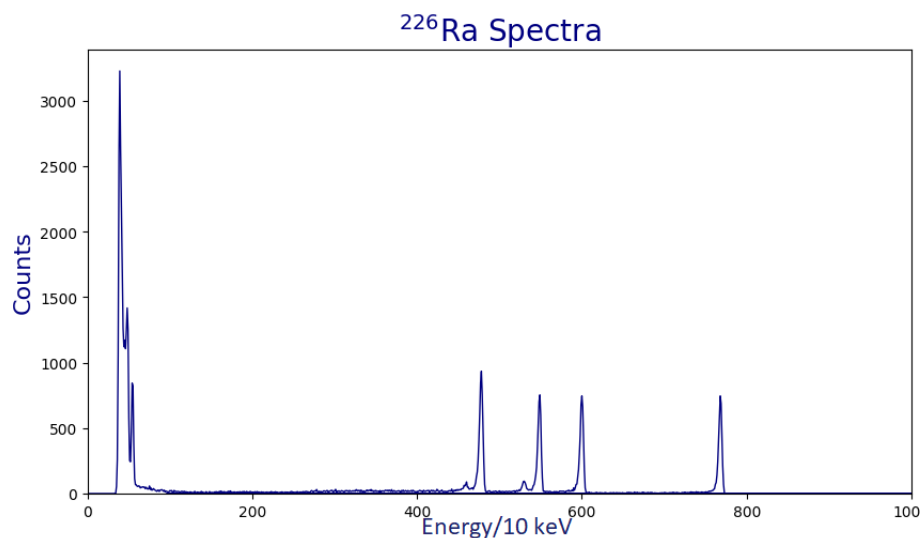


FIGURE 3.8: An example of the spectra of  $^{226}\text{Ra}$  that was used for calibration.

Figure 3.8 is the spectrum for charged particle calibration using the data from table 3.2. The four peaks on table 3.2 are visible at the far right of the spectrum. These are the signature peaks of the  $\alpha$  emission line originating from  $^{226}\text{Ra}$  decay chain.

Next time spectra alignments and add-back corrections were done. The specifics of how add-back is performed is discussed in the following chapter when add-back is carried out for the silicon detector. Figure 3.10 is an example of the spectra of the time spectra that was used, and shows the time spectra before the alignment and after alignment was accomplished. Figure 3.11 shows the time spectra after the alignment was carried out. The aligned time spectra was used to construct particle- $\gamma$  and particle- $\gamma$ - $\gamma$  coincidence events.

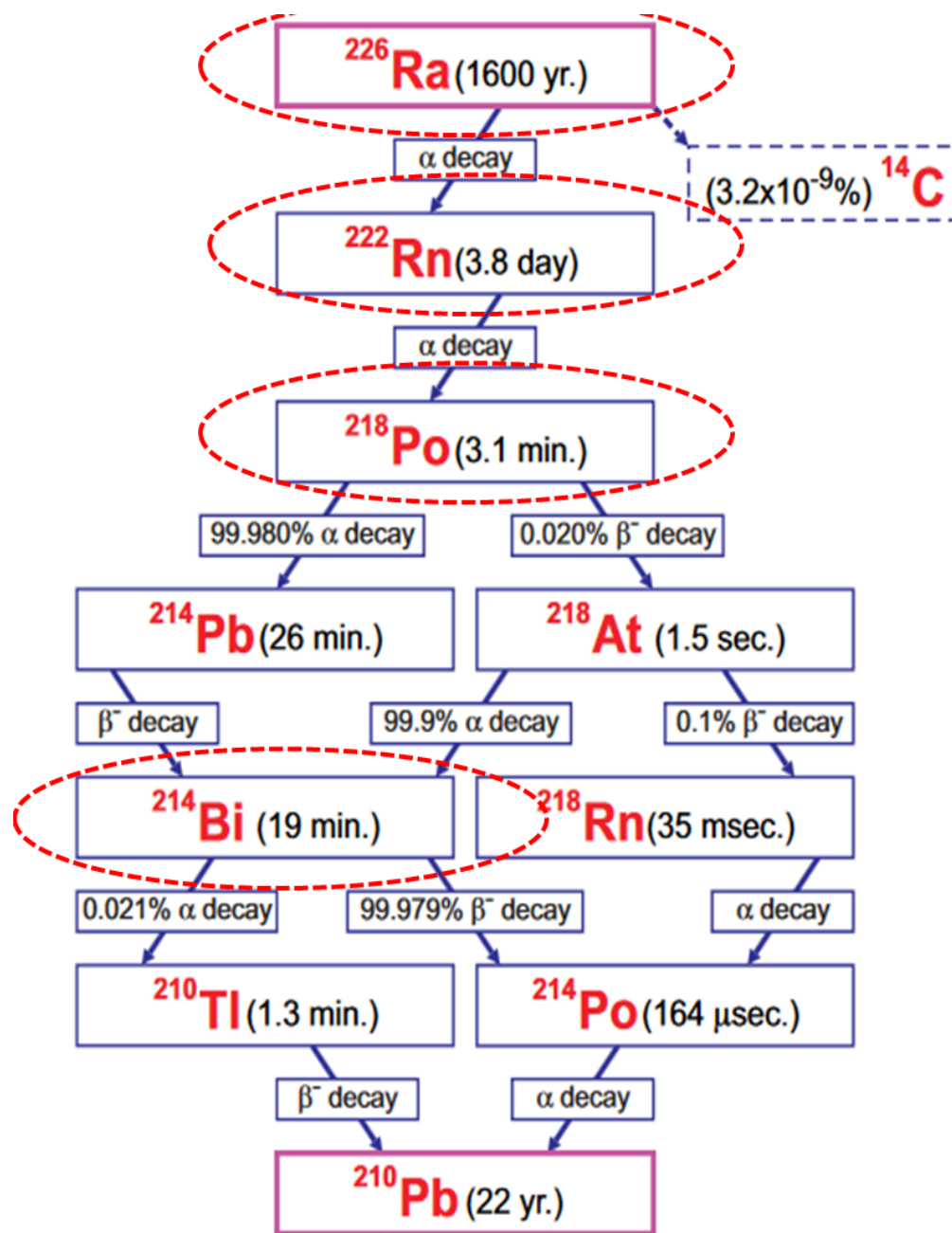


FIGURE 3.9: A schematic representation of the decay chain of  $^{226}\text{Ra}$  [28]. The four dashed ellipsoids represent the nuclei from which the alpha peaks originate in figure 3.8.

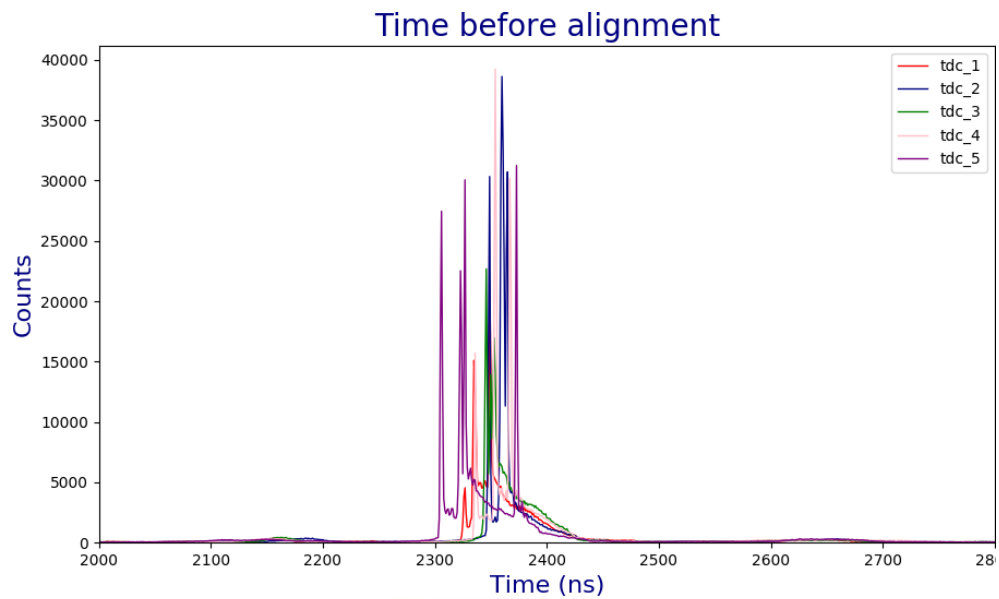


FIGURE 3.10: A representation of the time spectra before spectral alignment and add-back as read by the data acquisition system from the TDC.

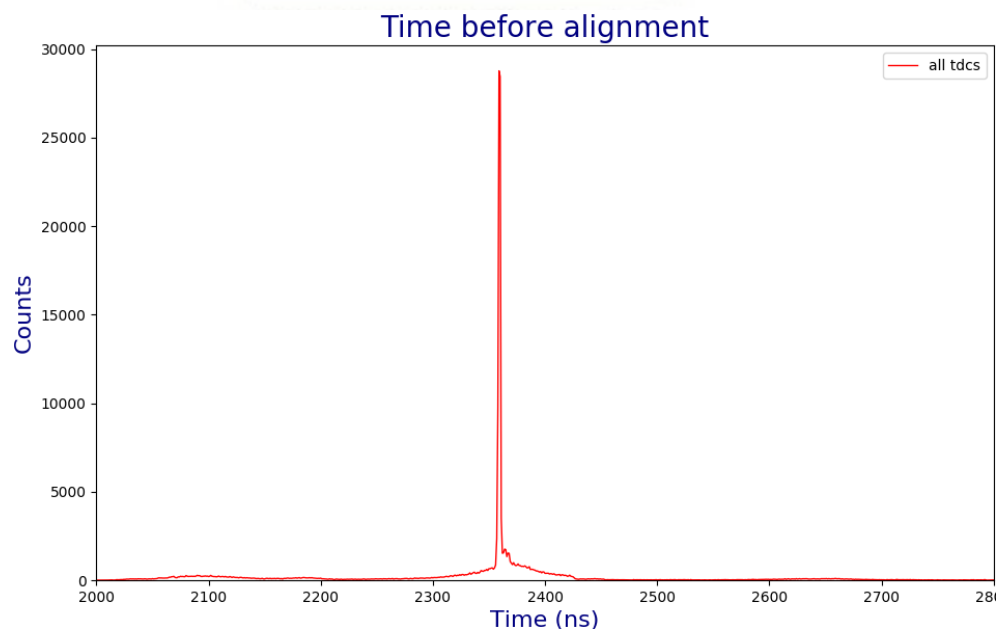


FIGURE 3.11: A representation of the time spectrum after all single time spectra are aligned and add-back is completed.

# Chapter 4

## Analysis

### 4.1 Software For Sorting and Displaying Histograms

The first part of this project was dedicated to developing and modifying a sort code written in C, which is dedicated to reading and interpreting the data discussed in this thesis. The software packages PRETSCAN [29] and TSCAN [29], from GPACK [29], and DAMM [30] were used which all worked together with the script that was written to extract information from the data.

The script was ran through PRETSCAN, which is a pre-processor for TSCAN. The C script, which is known as a usersub by the software TSCAN, contains a special block at the top, which is called preprocessing header. This block defines the types and sizes of my histograms and matrices, and also contains statements to process event words. Histograms and matrices are one dimension and many dimension plots, respectively. PRETSCAN uses the preprocessing header block to create proper data files and functions, by creating two preprocessing files, namely “matvar.h” and “initmatr.c”. The “matvar.h” file contains all the histogram and matrix variables and data incrementations, and “initmatr.c” contains all the information about the spectra to be plotted.

TSCAN is a software used to read raw data from tape or disk. It allows to do in-core 1-D histogram, 2-D and even 3-D matrices. It is used to unpack raw data and save it as either a histogram or matrix file, depending on how much variables are used, which is plottable as spectra. The script was written in C, and inputted

into TSCAN to get a matrix file of all the events in the data repacked in order.

The files `matvar.h` and `initmatr.c`, created by PRETSCAN, and the C script are used by TSCAN to do the data extraction and plotting of spectra. TSCAN outputs histogram files, and the histogram files are read and plotted using the software DAMM. DAMM is a Display, Analysis and Manipulation Module used to manipulate spectra.

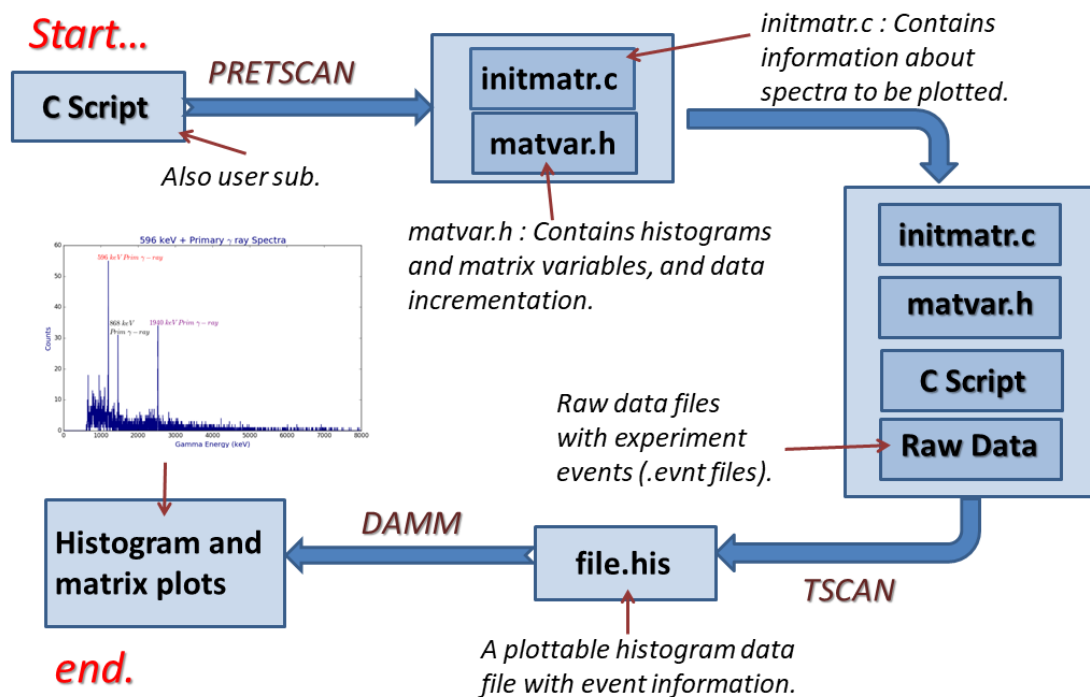


FIGURE 4.1: A step by step schematic representation of how the software work together to create histograms and matrix plots that are used for the analysis.

Figure 4.1 is a schematic representation of the steps taken from unpacking the C code script to plots of histograms and matrices for data analysis.

The second part of the analysis was to use the charged particles to specify my entrance excitation energies. This required doing some cleanup of the particle data, especially of random events and multiple hits on the rings and sectors by one particle. The following sections focus on particle and  $\gamma$  ray analysis.

## 4.2 Particle Analysis

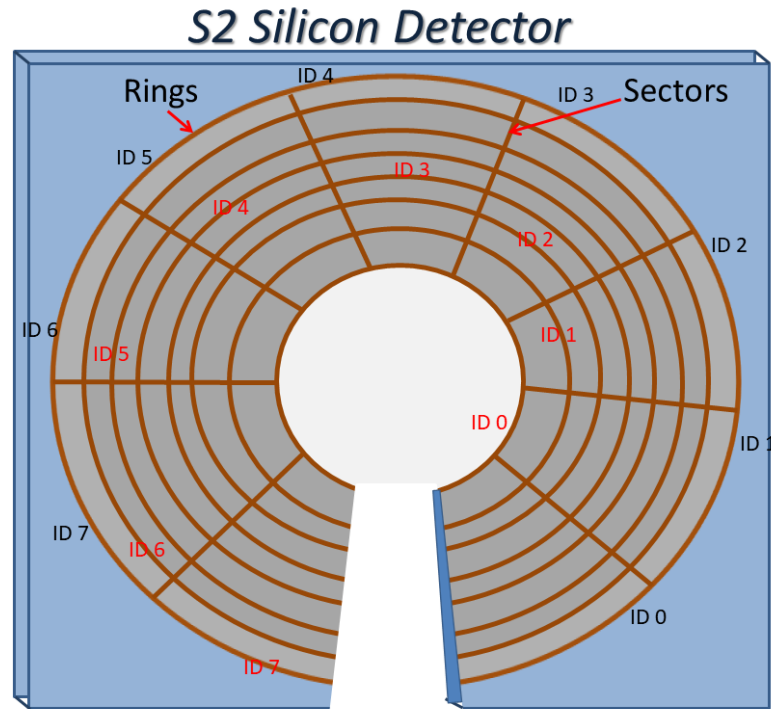


FIGURE 4.2: A schematic example of an S2 Silicon Detector.

Figure 4.2 is an example of the *S2* silicon detector used for particle identification. The rings form circular orbits around the center of the detector and the sectors form perpendicular lines going over the rings. Each ring or sector is denoted as an ID on the sort code. For the rings, ID 0 is the inner ring, the second one being ID 1, the third being ID 2 up to the outer most which is ID 23. The sector ID counting starts with the one on the right hand side near the opening, with it being ID 0. The one next to it, going anti-clockwise, is ID 1 up to the one on the left hand side being ID 7.

Figure 4.3 is a schematic diagram showing how particle ray tracing is done. The angle subtended by the inner ring from the target, using the beam line as a point of reference, is  $\theta_{lab} = 49^\circ$  and the last one stretches up to  $\theta_{lab} = 75^\circ$ . Ray tracing is done for rings and sectors separately. For the rings a requirement is performed on the code that if the charged particle hits on ring ID  $n$  on the front telescope, then take a hit on ring ID greater than  $n + 1$  and less than  $n + 5$  on the back telescope. These requirements mean that one cannot use the last 7 rings on the front detector, since there are no corresponding back rings to do the ray tracing

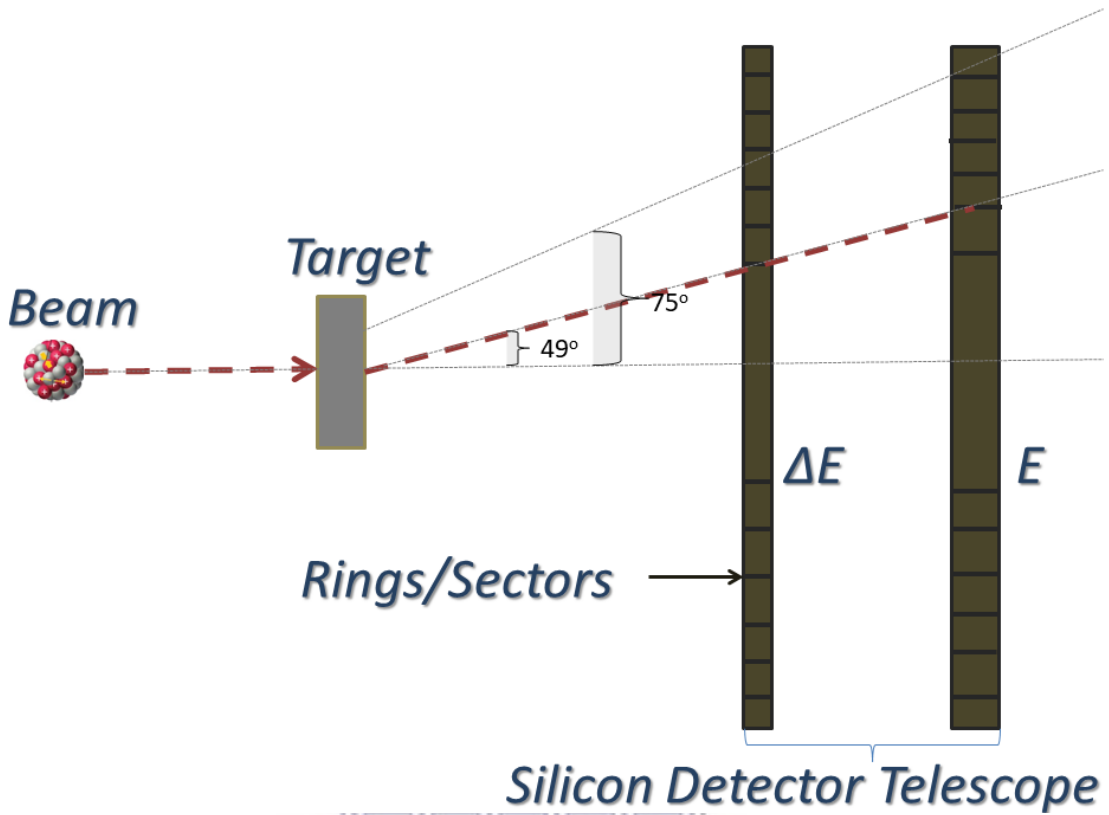


FIGURE 4.3: Schematic of particle ray tracing performed on the Silicon Detector Telescope.

with. The first 3 front rings were also omitted, because they had low statistics due to the bad design of the silicon setup frame. The tunnel cutting at the middle of the SDT had a spacing of 8.7 mm between the aluminum foil and the front silicon detector, which meant the first 3 inner rings were shadowed off from the experiment. Since It is required that the back rings start at ID greater than  $n + 1$ , so the back rings only start at ID 5.

Since the sectors are back to back, the lower IDs of the front sectors are in conjunction with the higher IDs of the back sectors. Hence the requirement was ID  $m = \text{ID}(6-m), \text{ID}(7-m), \text{ID}(8-m)$ . This means a hit on the front sector of ID 0, will hit the back sectors with ID 6, ID 7, ID 8, and a hit on the front sector of ID 1 will hit the back sectors with ID 5, ID 6, ID 7, and so on.

Figure 4.4 is a 2-Dimensional (2-D) plot of sector IDs. The vertical coordinates represent the back sector IDs and the horizontal coordinates represent the front sector IDs. Each coordinate on the spectra represents two sectors, one from the



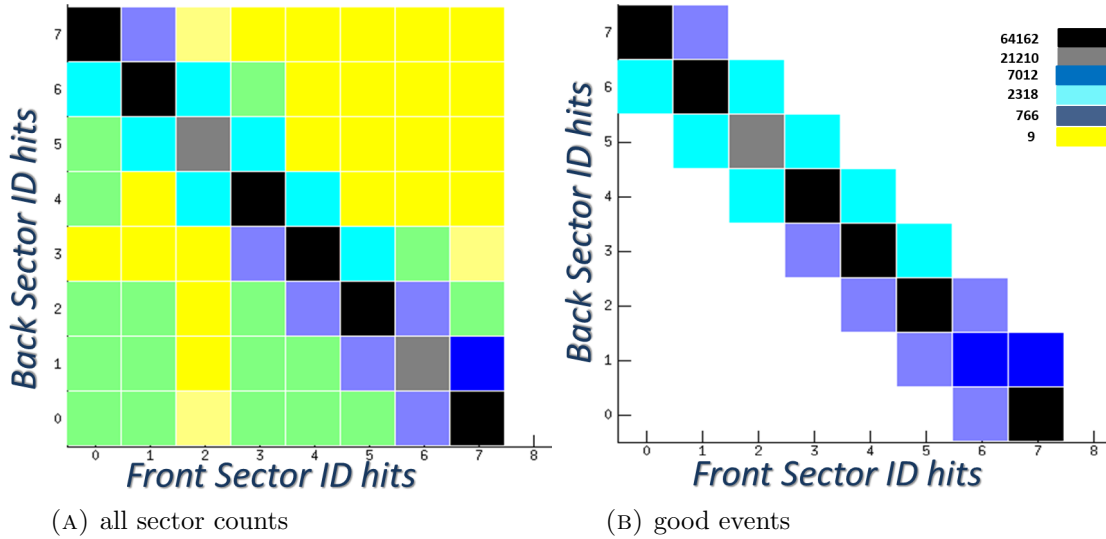


FIGURE 4.4: The sector count spectra created from each interaction with the SDT. The figure on the left (A) shows the events before charged particle ray tracing while the one on the right (B) shows the events after charged particle ray tracing.

front and one from the back detector, of many particle single full events with a time gate of 100 ns.

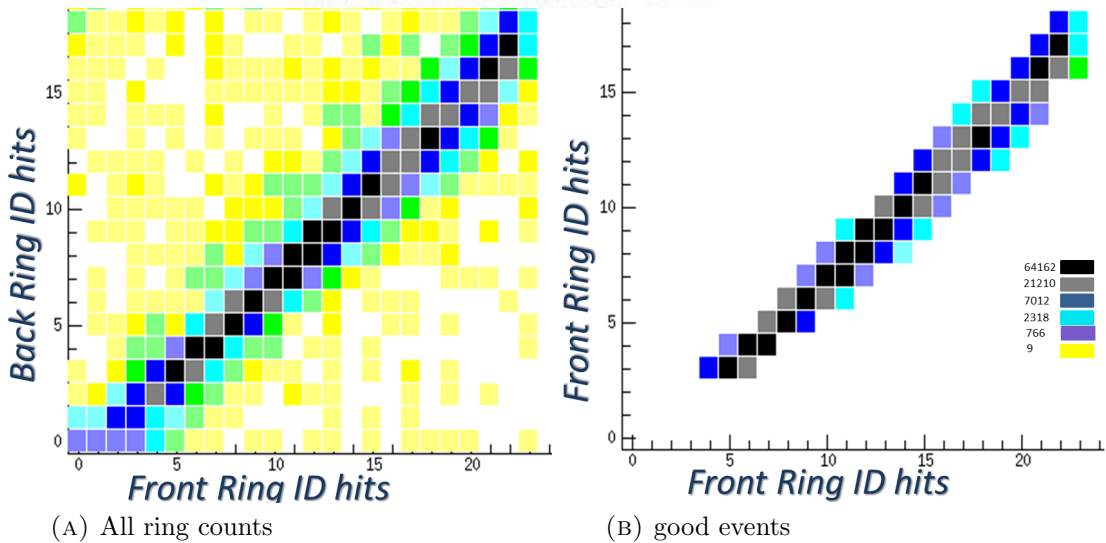


FIGURE 4.5: The ring count spectra created from each interaction with the SDT. The map shown in (A) is before charged particle ray tracing and the one shown in (B) is after charged particle tracing.

Figure 4.5 is a 2-D plot of ring IDs, with the vertical coordinates showing back ring IDs and the horizontal coordinates showing front ring IDs.

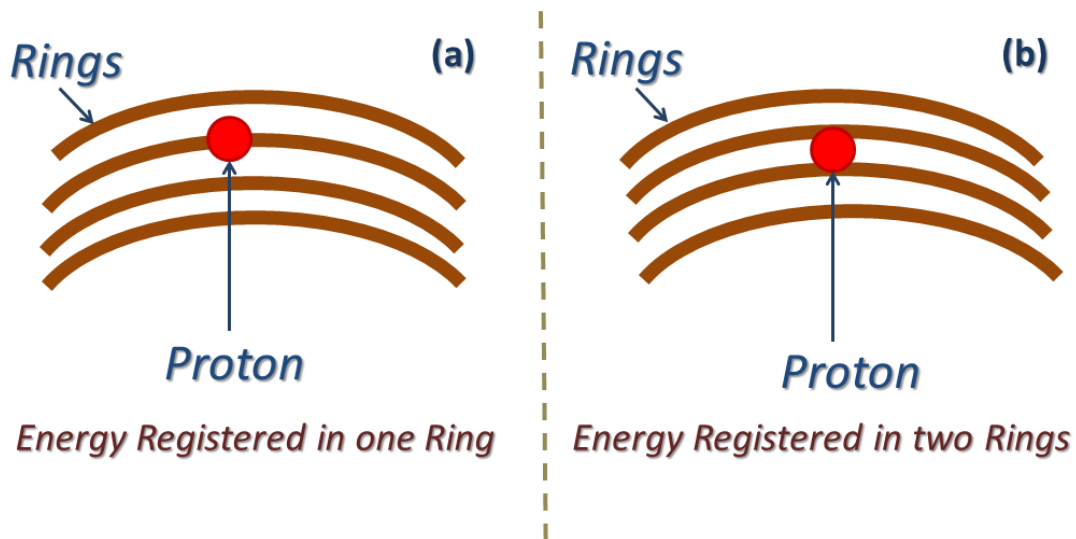


FIGURE 4.6: Schematic of energy sharing correction in adjacent rings.

The next correction that was carried out was the energy sharing correction. This is characterized by a single charged particle triggering more than one adjacent rings or sectors at a time. Figure 4.6 is a schematic representation of such events. Image (a) shows an event where the charged particle only hits one ring, while image (b) shows an image of a charged particle hitting two adjacent rings.

In cases such as the one on figure 4.6(b), where the charged particle hits more than one ring, there were more than one event counted, with each hit counting as an event. To solve this a condition was set such that if two adjacent rings fire at the same time, then the event is counted as one by adding up the energies of the two adjacent rings to give one total energy reading. If the energy on the first ring ID  $n$  is greater than that on the second ID  $n + 1$ , the event is counted as belonging to the first ring with ID  $n$ . Else if the ring with ID  $n + 1$  has a larger energy deposited on it than ring ID  $n$ , then the event is set to belong to the second ring of ID  $n + 1$ .

Energy sharing correction for more than two hits from one particle were also done. The same procedure as for two hits was performed for more than two hits, taking only events where adjacent rings fire, add the energies together and take the event to belong to the ring with the highest energy registered. The lowest

energy limit that was taken for multiple hits was 100 keV and if for an event with multiple hits, none of the energy readings on the rings was greater than 100 keV, then that event was discarded.

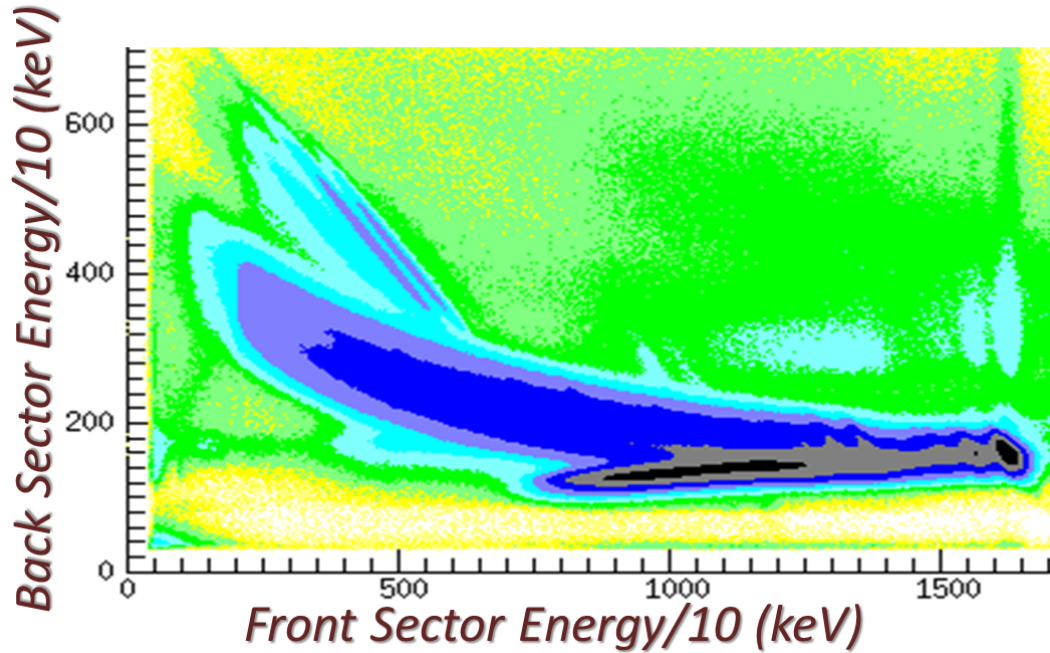


FIGURE 4.7: 2-D spectra for back sector energies against front sector energies.

corrections were also done for the sectors, but because the gap between the sectors was considerably larger than the gap between the rings, only the energy sharing correction for two hits from one particle was performed. The same logic as in the rings for the two hits was followed.

Figure 4.7 is the spectra of charged particle (proton) identification. Each co-ordinate in the spectra represents the pixel energies of many single particle full events going from the front silicon sectors through to the back silicon sectors. The spectra contains a punch through which is as a result of protons which go through both the front and back silicon detectors, and hence since they leave with some of their energy, their energy cannot be resolved to the excited states of the nucleus that are below the separation energy.

Figure 4.8 is the spectra of protons going through the front and back rings. The punch through is also visible on the ring spectra. The lower excitation states are at the bigger energies, because this is the particle entrance excitation energy through

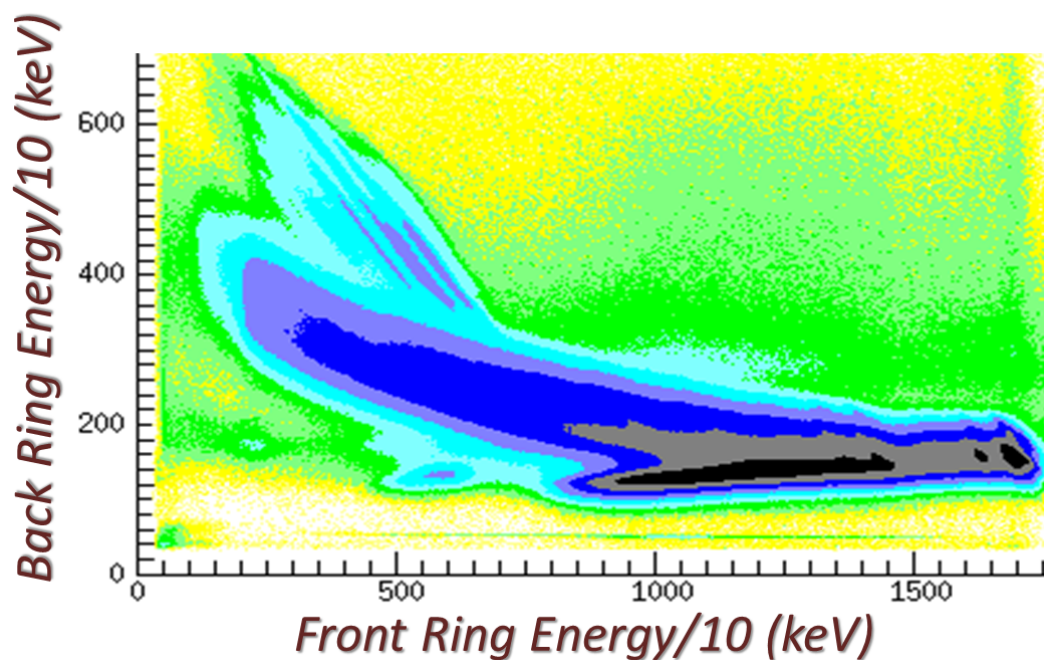


FIGURE 4.8: 2-D spectra for back ring energies against front ring energies.

the SDT, and thus has not yet been converted into proper excitation energy.

After all the corrections, one further step is needed before performing particle- $\gamma$  coincidences. That step is the free form gate or banana gate, which is shown in figure 4.9. The spectrum on the left is a spectrum of the  $^{74}\text{Ge}(p,p')^{74}\text{Ge}$  reaction channel with the  $^{74}\text{Ge}(p,d)^{73}\text{Ga}$  channel and punch through. The spectrum on the right is after a banana gate was applied, and only the  $^{74}\text{Ge}(p,p')^{74}\text{Ge}$  channel is visible. Estimation of when the punch through takes place for different angles was carried out and then the banana was set accordingly.

For the rest of this chapter and the following chapters, use of the spectra on the right hand side for coincidence reactions on figure 4.09 is carried out, with the reaction channel coming only from  $^{74}\text{Ge}(p,p')^{74}\text{Ge}$ . Even though the punch through is part of the reaction channel  $^{74}\text{Ge}(p,p')^{74}\text{Ge}$ , it is still removed because it does not resolve to any of the excited states of the nucleus.

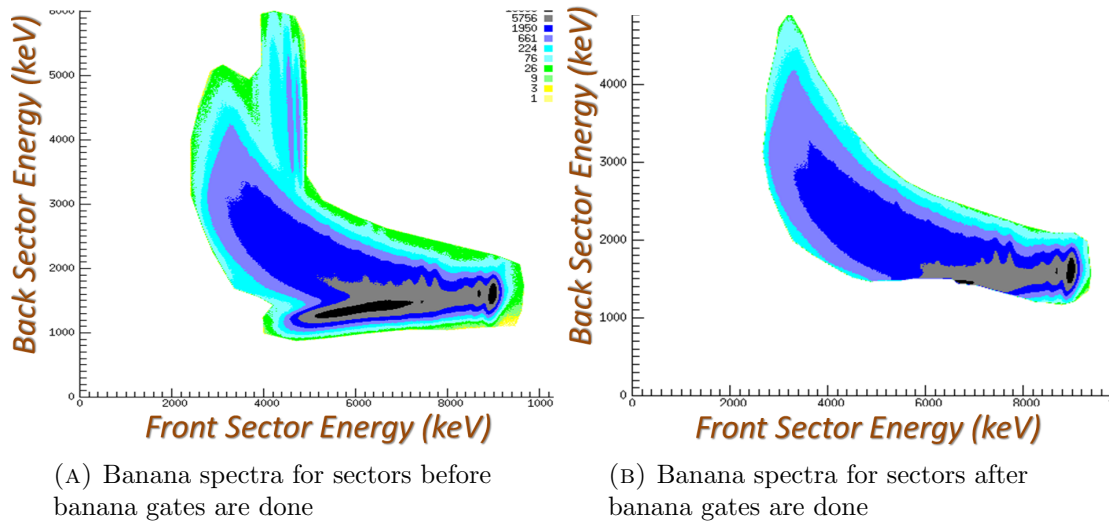


FIGURE 4.9: Particle- $\gamma$  gated banana spectra for sectors. (A) is the spectra before the banana gates to suppress all the other channels besides  $^{74}\text{Ge}(p,p')^{74}\text{Ge}$  and punch through. (B) is the spectra after the suppression is done and only the  $^{74}\text{Ge}(p,p')^{74}\text{Ge}$  channel is visible.

### 4.3 Energy Corrections

The conversion from particle energy to excitation energy involves using the beam energy, 18 MeV, and subtracting from it the charged particle energy measured by the SDT, which is the energy shown on the 2D scatter plot on figure 4.7 and figure 4.8, and some energy correction terms. Energy corrections will be discussed fully in this section. The following formula is used to specify the entrance excitation energy

$$E_{ex} = E_{beam} - E_{sil} - E_{al} - E_{Recoil} - Q_{value} . \quad (4.1)$$

$E_{beam}$  is the beam energy with value of 18 MeV.  $E_{sil}$  is the energy as measured by the SDT.  $E_{al}$  is the energy deposited in the aluminum foil put in front of the SDT and  $E_{Recoil}$  is the energy transferred to the recoiling of the nucleus.  $Q_{value}$  is the Q-value, but is zero for this reaction.

The first energy correction performed was for the foil put in front of the SDT. The aluminum foil was put in front of the SDT to protect it from delta electrons,



and was  $12.5 \mu\text{m}$  thick. The equation used for the energy transferred to the aluminum foil was,

$$E_{al} = \frac{dE}{dx}[E_{sil}] \frac{D_{al}}{\cos \theta [ID_{front\_ring}]}, \quad (4.2)$$

where  $\frac{dE}{dx}[E_{sil}]$  is the stopping power of aluminum foil calculated at different particle energies.  $E_{sil}$  is the charged particle energy registered by the SDT.  $D_{al}$  is the thickness of the aluminum foil, which is  $12.5 \mu\text{m}$ , and  $\cos \theta [ID_{front\_ring}]$  is the term relating the distance from the target to  $S2$  and the angle subtended by the protons from the line of incidence of the beam to the first ring, up to the final ring.

Figure 4.10 is a schematic diagram showing the variable labeling used in the equations.

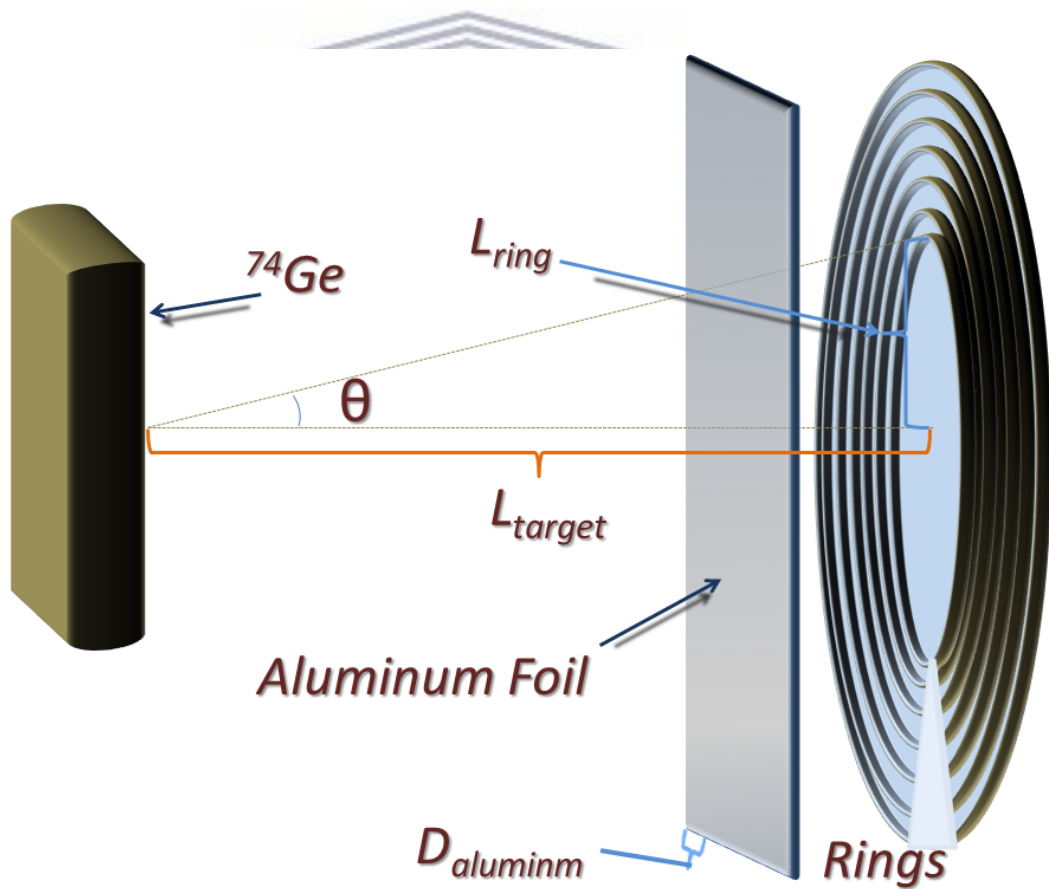


FIGURE 4.10: Schematic of the recoil correction for aluminum foil.

The second energy correction was for recoil energy of the nucleus  $^{74}\text{Ge}$ . I used the following formula for the recoil correction,

$$E_{Recoil} = \frac{M_b}{M_t} E_b + \frac{M_{ej}}{M_t} E_s - \frac{2}{M_t} \sqrt{M_{ej} M_b E_b E_{sil}} \cos \theta \quad , \quad (4.3)$$

where  $M_b$  is the mass of the charged particle, which is the proton mass.  $M_t$  is the mass of the target, which is the  $^{74}\text{Ge}$  nucleus.  $M_{ej}$  is the mass of the ejectile, which in this case is the proton mass.  $E_b$  is the beam energy, which is 18 MeV, and  $E_{sil}$  is the energy that is measured using the SDT shown in the banana energy spectra.  $\theta$  is the angle that the proton ejectile direction makes with the beam direction as shown in figure 4.11.

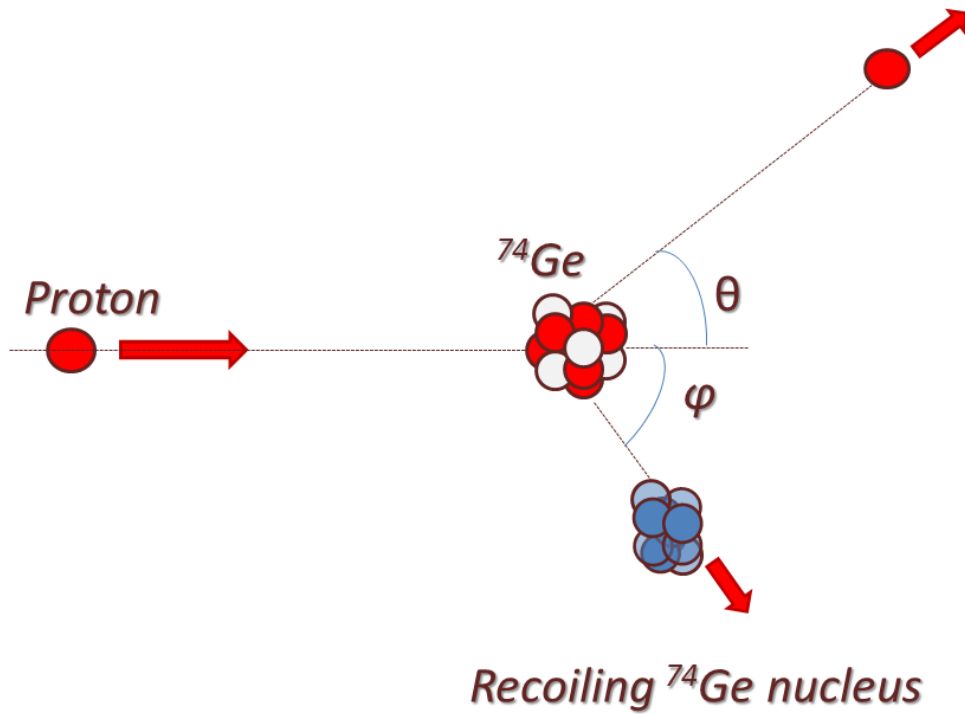


FIGURE 4.11: Two body kinematics of a proton projectile and a  $^{74}\text{Ge}$  nucleus.

Figure 4.11 is a schematic representation of how a typical two body kinematics reaction works. When the incoming beam interacts with the target nucleus, not only does it excite the nucleus, but it also transfers some of its momentum in the nucleus. This results in the nucleus being scattered at an angle  $\phi$ , and thus leaving with some of the projectiles energy.

The projectile also loses some of its energy when passing through the target and the dead layer of the detectors. This energy loss however is not accounted for in this analysis. That is because the energy loss through these layers has little effect on the results of the overall analysis.





## 4.4 $\gamma$ -ray Analysis

$\gamma$ -ray energy sharing corrections were also carried out, where when two adjacent diodes fire at the same time, the two energies are added up and made to a single event.

Figure 4.12 is a spectrum of excitation energies. the particle entrance energy in the silicon telescopes is converted to excitation energy using equation (4.4). The neutron separation energy ( $S_n$ ) for the nucleus  $^{74}\text{Ge}$  is 10.20 MeV [27].

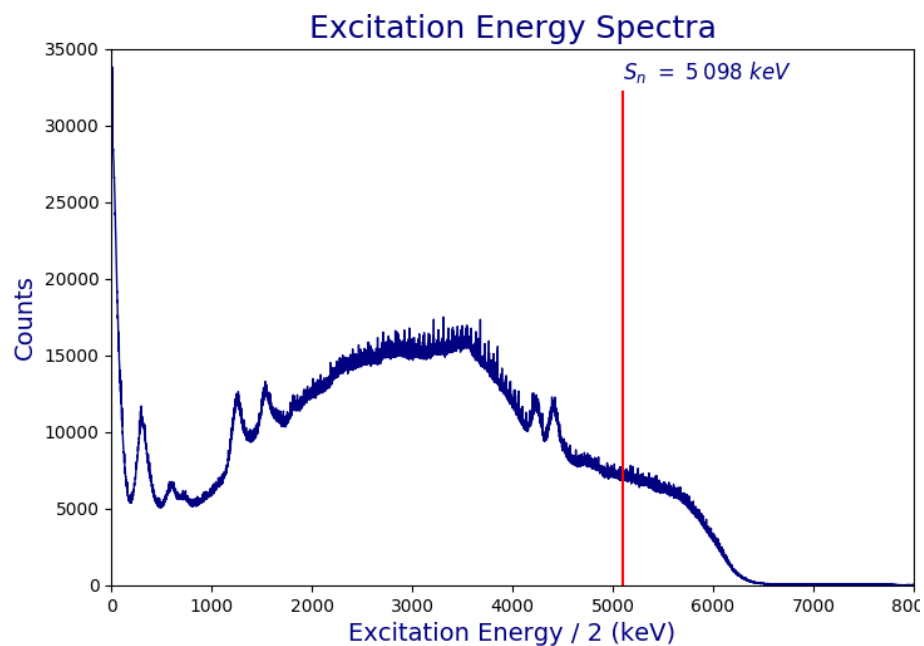


FIGURE 4.12: Energy spectrum from  $^{74}\text{Ge}(p,p')^{74}\text{Ge}$  reaction

Figure 4.13 is a  $\gamma$ -ray energy spectra of the  $\gamma$ -rays emitted by the nucleus up to 2 MeV. I use the  $\gamma$  rays from this spectra to make particle- $\gamma$  and particle- $\gamma$ - $\gamma$  coincidences.

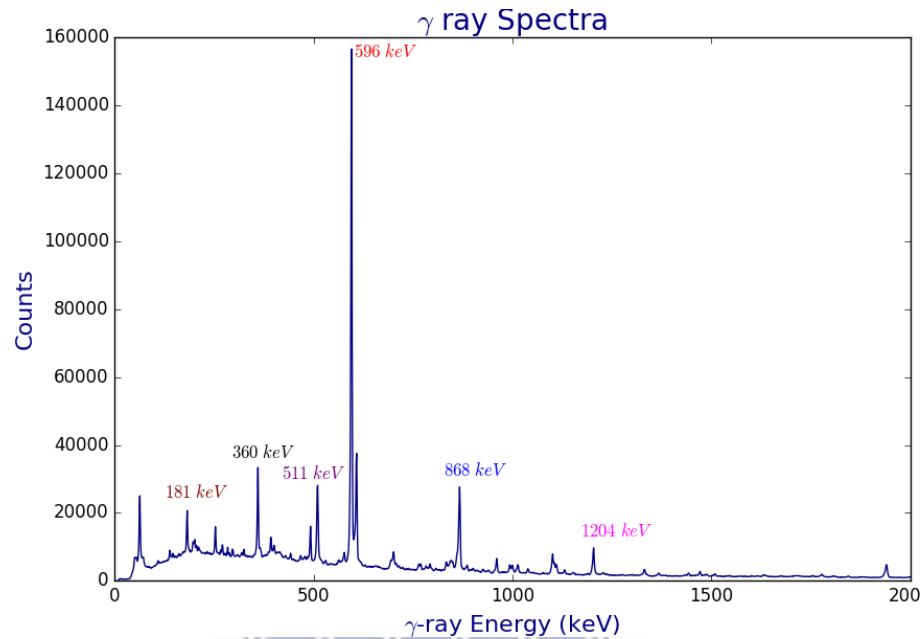


FIGURE 4.13: Excitation energies after recoil and aluminum foil energy loss corrections up to 2 MeV. The peak with the highest counts is the 596 keV  $\gamma$ -ray which belongs to the first excited state of the nucleus.

The first excited state has the highest counts because most of the  $\gamma$  rays from the quasi-continuum cascade down to this state. I have also shown the 1204 keV  $\gamma$  ray which belongs to the second excited state decaying straight to the ground state. Both the first and second excited states have spin and parity of  $2^+$ .

Figure 4.14 is an excitation energy versus  $\gamma$ -ray energy 2-D coincidence spectra. It shows the  $\gamma$  rays feeding into the different energy states of the nucleus. The strongest transition as observed from the diagram is the 596 keV  $\gamma$ -ray emission from the first-excited state. The excitation energy lines on the spectra get more dense as the excitation energy increases.

The main objective from this point on is to extract particle- $\gamma$ - $\gamma$  coincidences using the information in figure 4.14. To achieve this goal, I first put a gate on particle excitation energies from the particle singles events. I then set the first  $\gamma$ -ray gate on the  $\gamma$  from a state with a specific spin and parity, decaying to the ground state. I set a gate on the second  $\gamma$  ray such that the first and second  $\gamma$  rays add up to

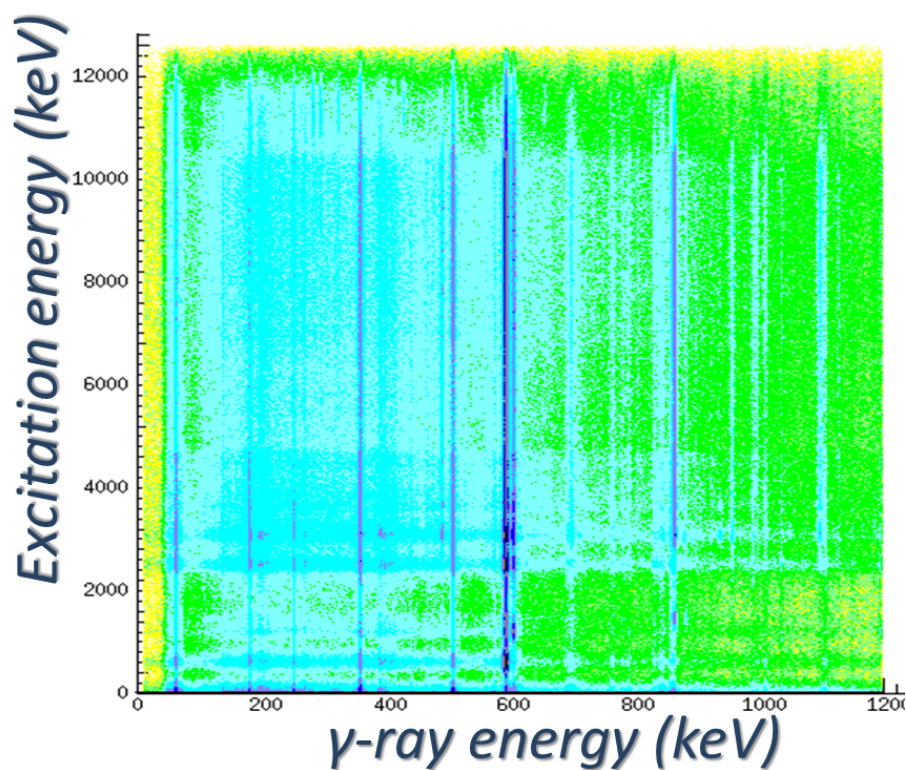


FIGURE 4.14: Particle versus  $\gamma$ -ray energy spectra.

the particle excitation energies.

Figure 4.15 is a schematic diagram showing one of the particle- $\gamma$ - $\gamma$  coincidences made. Started off by setting a gate on excitation energy. Next I applied a  $\gamma$ -ray gate on the level state of energy 596 keV with spin  $2^+$  and required that the 596 keV added to the primary  $\gamma$  ray adds up to the excitation energy at the quasi-continuum region.

With this condition I was able to make a spectra of all the primary  $\gamma$  rays that feed to the 596 keV level state together with the 596 keV  $\gamma$ -ray, i.e, a plot of counts vs (596 keV + primary  $\gamma$  ray) . Figure 4.16 is such a spectra. Since the two  $\gamma$  rays add up to the different excitation energies of the nucleus, so this is a spectra of excitation energies built on top of the 596 keV state.

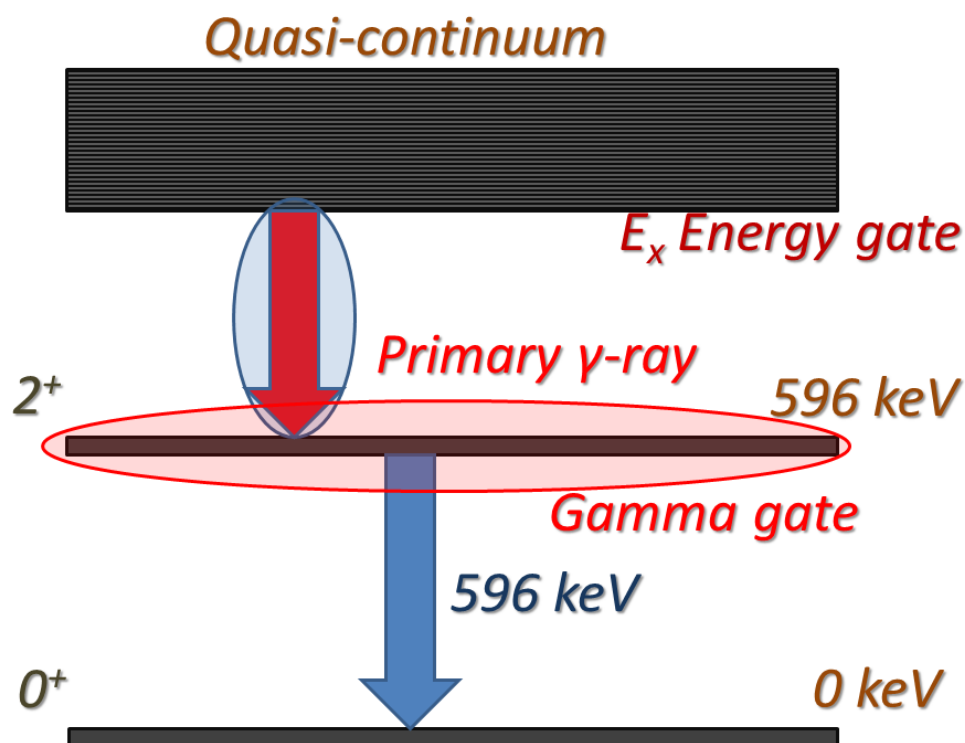


FIGURE 4.15: A schematic representation of how particle- $\gamma$ - $\gamma$  coincidences are done. A gate in excitation energy at the quasi-continuum is applied, followed by a gate on a secondary  $\gamma$ -ray that decays to the ground state. A primary  $\gamma$ -ray is required to come from the quasi-continuum and feed into the state of the secondary  $\gamma$ , which is the 596 keV level state in this case.

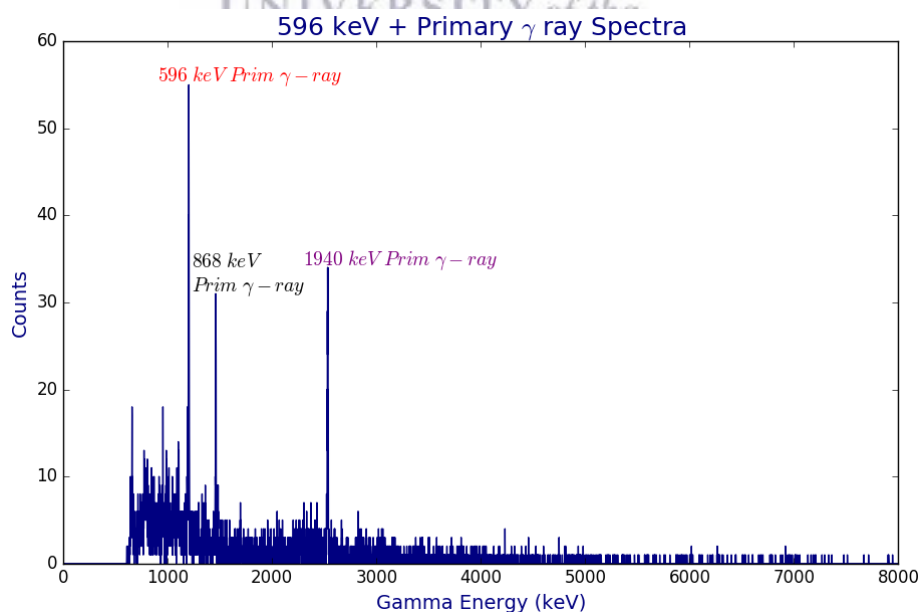


FIGURE 4.16: The primary  $\gamma$ -rays that are coming out of the quasi-continuum and feeding directly into the 596 keV state.

## 4.5 Efficiency Calibration for HPGe Detector

Energy efficiency calibrations were also accomplished for the HPGe detectors using the  $^{152}\text{Eu}$   $\gamma$ -ray source. The energy peaks shown in table 3.1 on the first column were used. The software Ecal was used to get the efficiency parameters and then used them to make  $\gamma$ -ray intensity corrections.

In the first few runs of the experiment,  $^{13}\text{C}$  and  $^{14}\text{C}$  runs were executed for the efficiency calibration. Efficiency calibration was performed using particle- $\gamma$  coincidences. Table 4.1 is a table of the  $^{14}\text{C}$  data. Use of  $^{152}\text{Eu}$  for low energies is done and  $^{13}\text{C}$  and  $^{14}\text{C}$  are used for high energies.

$^{14}\text{C}$  efficiency calibration data.

energy (keV)	area
613.0	14671.0
1248.0	17634.0
6092.4	8527.0
6726.0	1254.0

TABLE 4.1:  $^{14}\text{C}$  transition anergies that were used for efficiency calibration. The first column is the energy of the peak ( $\gamma$ -ray) and the second is the area under the peak.

Figure 4.17 shows a  $\gamma$ -ray spectrum of  $^{14}\text{C}$  from 2 to 8 MeV, and only two  $\gamma$  peaks are shown out of the four peaks that were used. The area under each peak is given in column 2 of Table 4.1.

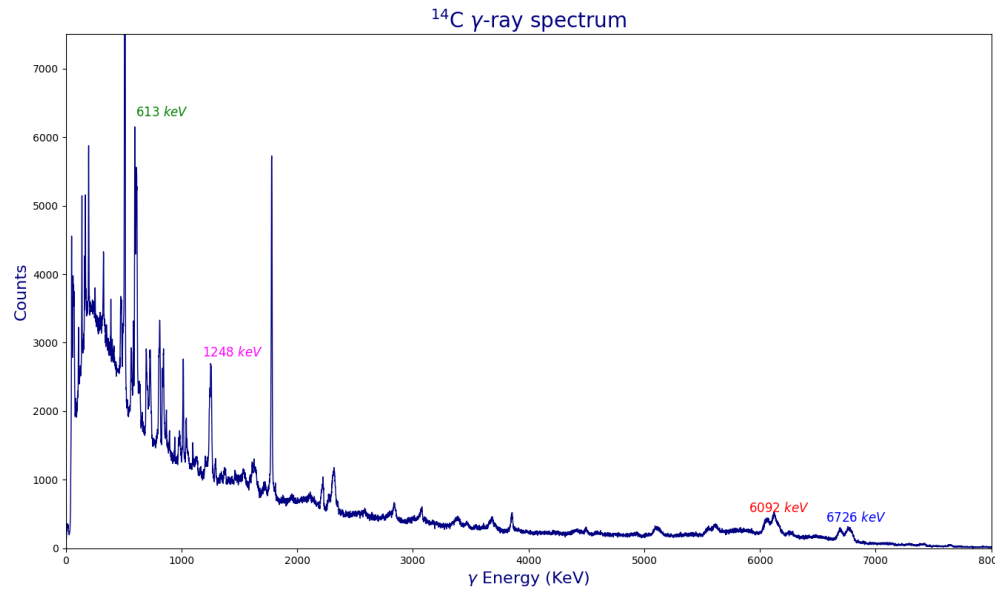


FIGURE 4.17: Two  $\gamma$ -rays that were used for efficiency calibration coming from  $^{14}\text{C}$ . The spectrum shows the energy range between 2 and 8 MeV.

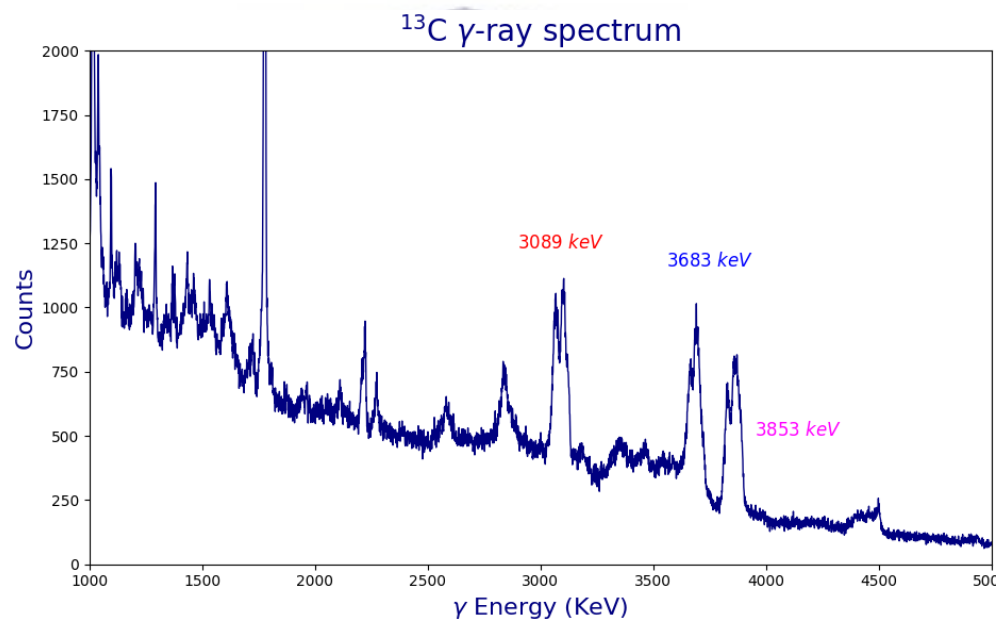


FIGURE 4.18: Three  $\gamma$ -rays that were used for efficiency calibration coming from  $^{13}\text{C}$ .

Figure 4.18 is the  $\gamma$ -ray spectra of  $^{13}\text{C}$  from 0 to 5 MeV. The three  $\gamma$  peaks, 3.089 MeV, 3.683 MeV and 3.853 MeV, are the peaks that were used for efficiency calibration from  $^{13}\text{C}$ . All the peaks that were used from the carbon isotopes were split into half. That was due to the Doppler effect which was magnified at high energies as a consequence of the formula  $E_{DS} = E_{\gamma}(1 + \frac{v}{c} \cos \theta)$ , where  $v$  is the velocity of the recoil nucleus, which was the one of the carbon isotopes in this case, relative to the detector and  $c$  is the speed of light.  $E_{\gamma}$  is the energy of the

$\gamma$  ray decaying from the recoil nucleus,  $\theta$  is the angle projected by the detector relative to the direction of the beam and  $E_{DS}$  is the Doppler shifted energy.

Although it would have been desirable to include a Doppler correction, for the sake of this work it was determined that the Doppler shifted spectra provides a sufficiently good value to proceed. This was confirmed by the measured efficiency values which are consistent with those from previous work [1].

## 4.6 Results

After the analysis the spectra parameters are inputted for the particle- $\gamma$ - $\gamma$  coincidences and the efficiency parameters to calculate the strengths for each  $\gamma$ -ray transitions to well known low-lying spin states. The strength function ratios are extracted for states with spins  $0^+$ ,  $2^+$ ,  $3^+$ ,  $3^-$ , and  $4^+$ .

To extract the shape of the  $\gamma$ -ray strength function of the different states, one needs a way to go from excitation energy to primary  $\gamma$ -ray energy. To interchange from the excitation energy to primary  $\gamma$ -rays, we use the formula,

$$E_{prim} = |E_x - E_\gamma|, \quad (4.4)$$

where  $E_{prim}$  is the primary  $\gamma$ -ray energy we want to get.  $E_x$  is the excitation energy and  $E_\gamma$  is the  $\gamma$ -ray energy from the well known low lying state. Figure 4.15 shows clearly how this is done for the  $\gamma$ -ray energy from the 596 keV state. The calculations are done for two different primary  $\gamma$ -ray energy bins ( $\sigma(E_{primary})$ ), which are 120 keV and 200 keV respectively.

The energy efficiency for HPGe detector, as extracted using ecal, is given by this formula

$$\log_{10}[eff(E_{prim})] = a - b [\log_{10}(E_{prim})] + c [\log_{10}(E_{prim})]^2 - \frac{d}{(E_{prim})^2}. \quad (4.5)$$

To get the efficiency both sides must be exponentiated by base 10 to get.

$$eff(E_{prim}) = 10^{\log_{10}[eff(E_{prim})]} \quad (4.6)$$

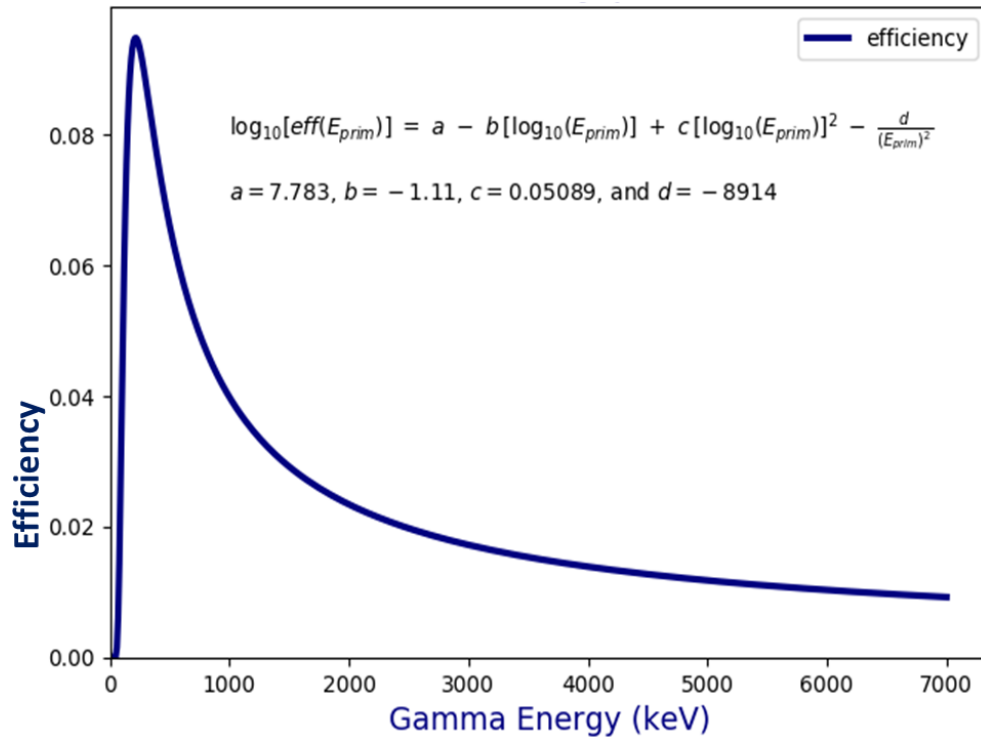


FIGURE 4.19: An efficiency plot for all the HPGe detectors which was measured from  $^{152}\text{Eu}$ ,  $^{13}\text{C}$  and  $^{14}\text{C}$ .

All the uncertainties were propagated to obtain the total uncertainty of the efficiency which amounts to 5% of the efficiency values.

Figure 4.19 is the efficiency plot obtained from using equation 4.6, from 0 keV up to 7 000 keV. The parameters  $a$ ,  $b$ ,  $c$  and  $d$  are obtained from inputting the data values for  $^{152}\text{Eu}$ ,  $^{13}\text{C}$  and  $^{14}\text{C}$  shown in table 4.1 into the software ecal which calculates the efficiency of the detector from the parameters in table 4.1. Europium and carbon combination was used because  $^{152}\text{Eu}$  has its highest  $\gamma$ -ray energy at 1408 keV, while the data goes up to 10 MeV in  $\gamma$  energy. To resolve the problem we use  $^{13}\text{C}$  which has its highest energy  $\gamma$ -ray at 3.089 MeV and  $^{14}\text{C}$  which has its highest energy  $\gamma$ -ray at 6.726 MeV for the calibration. All the data was combined for  $^{152}\text{Eu}$ ,  $^{13}\text{C}$  and  $^{14}\text{C}$  into one table, and the data was fed into ecal to get the parameters  $a$ ,  $b$ ,  $c$  and  $d$  that were used in equation 4.5.



Efficiency calibrations were also performed for the  $\gamma$ -rays from the well known states that the primary  $\gamma$ -rays feed to, using equation 4.5.

To get the true primary  $\gamma$ -ray intensities, corrections for the counts were performed on the  $\gamma$ -ray peaks using the efficiency of the HPGe detector. First a correction was made on the primary  $\gamma$ -ray energy using the formula

$$Corr_{prim} = \frac{counts}{eff(E_{prim})} \quad , \quad (4.7)$$

and then did the same for the  $\gamma$ -ray from the well known state, using the equation,

$$Corr_{\gamma} = \frac{counts}{eff(E_{\gamma})} \quad . \quad (4.8)$$

To obtain the total primary  $\gamma$ -ray intensity the two intensities were multiplied and divided by the counts of the  $\gamma$ -rays, to obtain the equation

$$\begin{aligned} N_{L_{prim}} &= \frac{Corr_{prim} Corr_{\gamma}}{counts} = \frac{counts}{eff(E_{prim})} \frac{counts}{eff(E_{\gamma})} \frac{1}{counts} \\ &= \frac{counts}{eff(E_{prim}) eff(E_{\gamma})} \quad . \end{aligned} \quad (4.9)$$

The end product is an efficiency corrected primary  $\gamma$ -ray intensity. Using information from equation 4.4 and the one from equation 4.9, the construction of partial strength functions or *Quasi*<sup>1</sup> was performed for all the primary  $\gamma$ -ray energies feeding to each of the low lying well known states. They were constructed as follows,

$$df(E_{prim}) = Quasi = \frac{N_{L_{prim}}}{E_{prim}^3} \quad . \quad (4.10)$$

Since the excitation energies cover an energy range between 1 keV and 10 000 keV, 1 000 keV or 1 MeV bins were created. That is the *Quasi* were grouped by adding them together from 500 keV up to 1500 keV, omitting out the first 500 keV, which

<sup>1</sup>*Quasi* is the intensity of the primary  $\gamma$  rays feeding into a state divided by the energy of those primary  $\gamma$  rays,  $Quasi = N_{L_{prim}}/E_{prim}^3$ .

constitutes the first bin. 1500 keV up to 2 500 keV constitutes the second bin and so on. The first 500 keV is left out because the first excited state of  $^{74}\text{Ge}$  is 596 keV.



# Chapter 5

## Discussion

### 5.1 Ratios

Since most states in the nucleus have more than one  $\gamma$ -ray decay branch, branching ratio corrections for such states were performed. The 1204 keV state is an example of such case, which can decay to the ground state, but can also form a cascade to the 596 keV state first before going to the ground state, releasing a 608 keV  $\gamma$ -ray in the process.

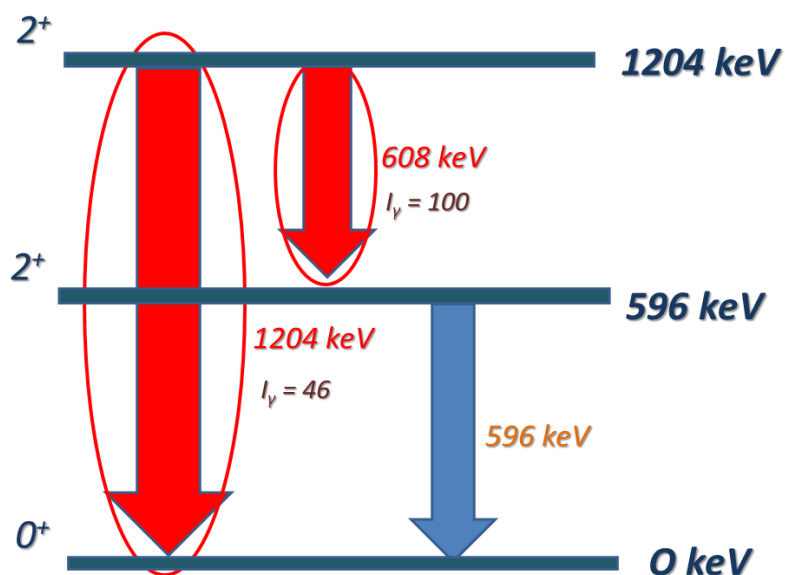


FIGURE 5.1: A schematic diagram of the branching ratio of the 1204 keV level decaying to the 596 keV and ground state.

Figure 5.1 is a schematic representation of how the 1204 keV state branching ratio correction is performed, which is the consideration of proportions of  $\gamma$ -rays decaying through different channels. The intensities shown on the diagram, taken from NNDC [27], were used to make the corrections as follows,

$$f(E_{608}) = \left( \frac{I_{608}}{I_{1204}} \right) f(E_{1204}), \quad (5.1)$$

where  $f(E_{608})$  is the intensity corrected Quasi of the 608 keV  $\gamma$ -ray state. As stated in the previous chapter, *Quasi* is the intensity of primary  $\gamma$  rays feeding into a state given by  $Quasi = N_{L_{prim}}/E_{prim}^3$ .  $I_{608}$  is the  $\gamma$ -ray intensity for the 608 keV  $\gamma$  ray and  $I_{1204}$  is the  $\gamma$ -ray intensity for the 1204 keV  $\gamma$  ray.  $f(E_{1204})$  is the *Quasi* of the primary  $\gamma$  rays that are feeding into the 1204 keV state.

To obtain the total *Quasi* strength of the  $\gamma$  rays coming out of the 1204 keV state, I add the corrected Quasi of the 608 keV  $\gamma$ -rays to the 1204 keV Quasi to get

$$f(E_{tot.1204}) = f(E_{1204}) + f(E_{608}). \quad (5.2)$$

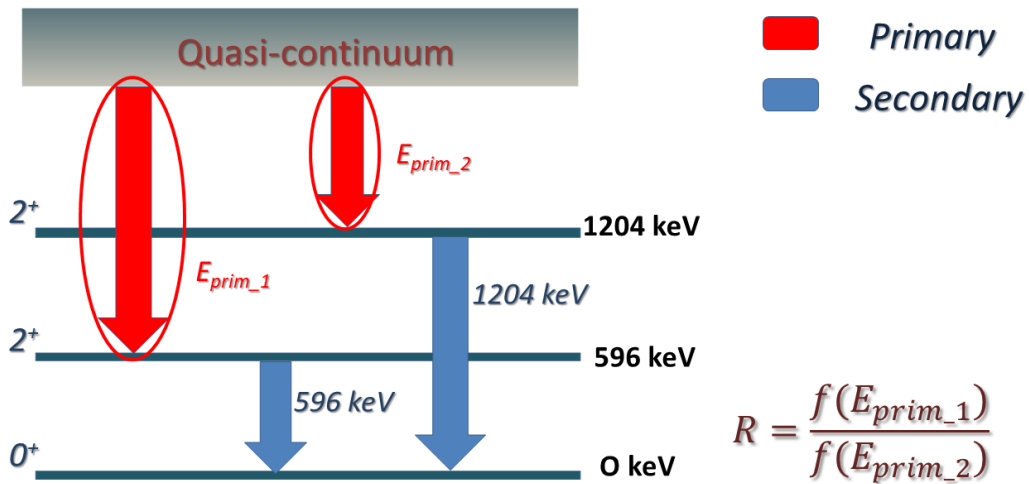


FIGURE 5.2: Ratios  $R = f(E_{596})/f(E_{1204})$  for primary  $\gamma$ -rays that feed into the 596 keV state over those that feed into the 1204 keV state.

Since the 596 keV  $\gamma$  ray is the only  $\gamma$  ray decaying from that state, there is no

branching ratio correction needed. Next I take the ratio  $R$  for the 596 keV *Quasi* over the 1204 keV *Quasi* to obtain,

$$R_{596\backslash 1204} = \frac{f(E_{596})}{f(E_{tot.1204})} \quad . \quad (5.3)$$

Figure 5.2 is a schematic diagram showing how this ratio is done and figure 5.3 is a data plot of the *Quasi* ratios of the 596 keV and 1204 keV excited states. The first gate is done on the 3 MeV excitation energy, with a deviation of  $\pm 0.5$  MeV, because the proton punch through occurs from 0 to 2.5 MeV. The *Quasi* ratio of the primary  $\gamma$ -rays coming from the 3 MeV excited state is taken that is feeding into the 596 keV excited state to the *Quasi* of the primary  $\gamma$ -rays coming from the 3 MeV excited state feeding into the 1204 keV excited state.

Next, a gate at 4 MeV excitation energy is applied and the ratio is taken again. The same is done for 5 MeV, 6 MeV, 7 MeV, and 8 MeV excitation energies, and the same ratios taken for all of them. The plot of the ratios against the excited states that were gated on is shown in figure 5.3.

As it is visible in figure 5.3, the plot starts from 3 MeV. That is because the punch through that was visible on the 2D scatter plot was calculated to be between 0 MeV and 2.5 MeV of the nucleus excitation energies. The punch through was calculated on the silicon telescopes using the software SRIM [31]. SRIM uses the information of stopping power of materials to calculate the distance a particle of certain energy and angular range travels in a target material using a quantum mechanical treatment of ion-atom collisions. A beam energy of 18 MeV was inputted together with parameters such as target thickness, aluminum foil in front of the silicon detectors and angular range of the beam.

SRIM calculated the proton punch through to be at 2.2 MeV of the nucleus excitation energy at  $\theta = 49^\circ$  and decreased with increasing angle up to  $\theta = 60^\circ$ , where it diminished to 0.0 MeV excitation energy. A margin of error on the calculations of up to 300 keV was allowed, and so started having confidence on the data from 2.5 MeV excitation energy. Each excitation energy point on figure 5.3 is 1 MeV wide, coming from the binning as explained in the previous chapter.

The plot on figure 5.3 is not the GSF, but is a ratio of *Quasi* strengths of two

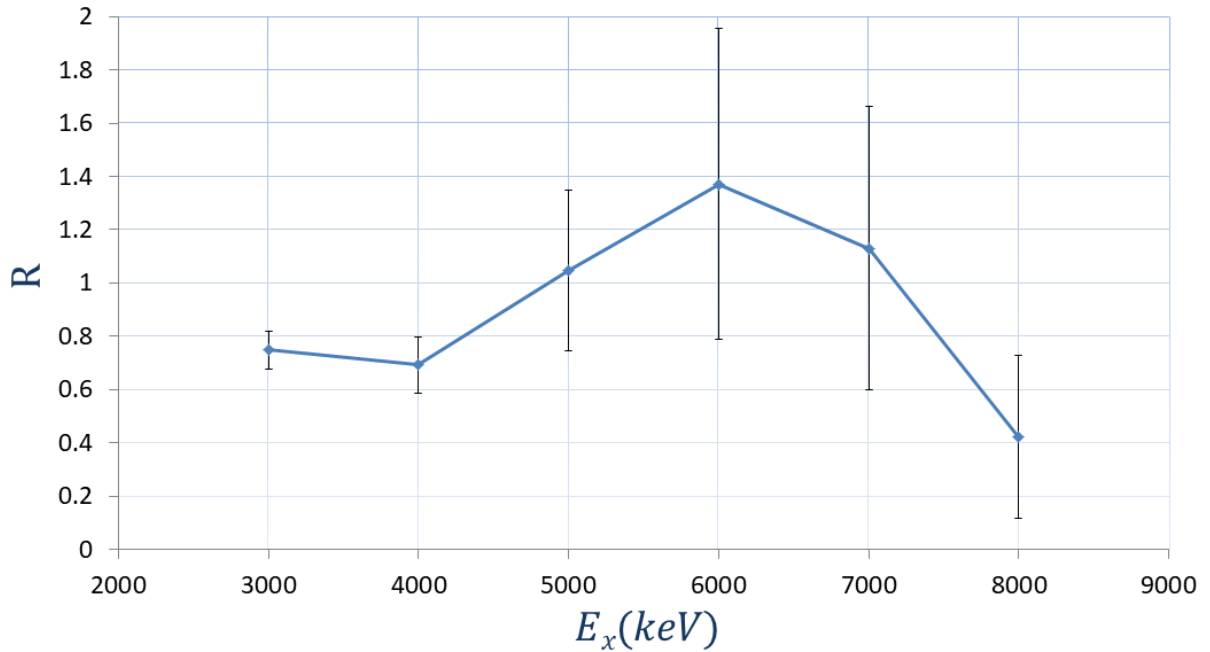


FIGURE 5.3: The ratios of the strength of primary  $\gamma$ -rays that are feeding into the 596 keV state against the strength of the primary  $\gamma$ -rays that are feeding into the 1204 keV state.

different states with the same spin, which is  $2^+$  in this case. This tells us about the shape of the GSF of the  $^{74}\text{Ge}$  nucleus.

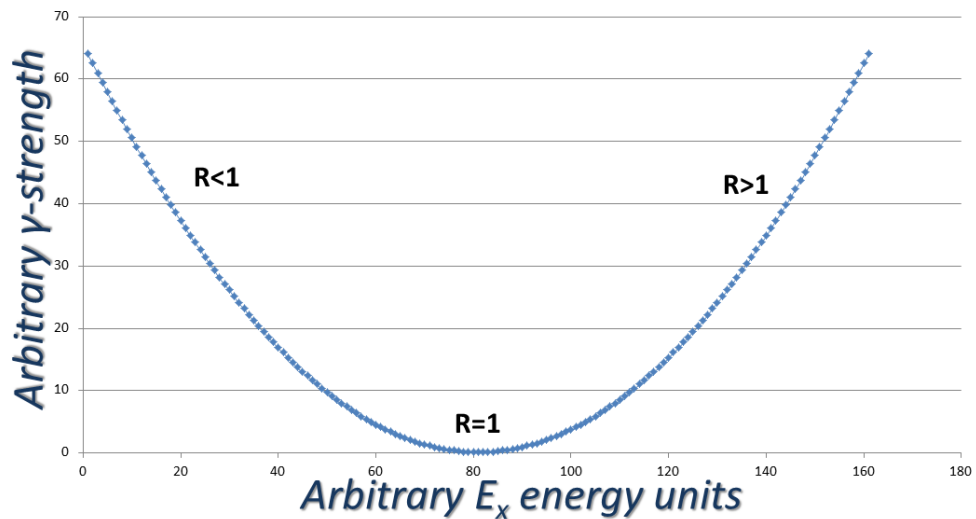


FIGURE 5.4: The shape of the GSF as depicted by the ratios.

For the parts that the ratio  $R$  is less than one corresponds to the part of the relative strength function where it is decreasing. The ratio is given as  $R = f(E_1)/f(E_2)$ , where  $f(E_1)$  is the relative strength of the primary  $\gamma$  ray decaying to the lowest energy level and  $f(E_2)$  is the relative strength of the primary  $\gamma$  ray decaying to the energy level higher than  $E_1$ . If  $R < 1$ , then it implies that  $f(E_1) < f(E_2)$ , which means at that region the GSF is decreasing.

For example in the ratio plot of  $f(596)/f(1204)$  in figure 5.3,  $R$  is less than one for  $E_x = 3000$  keV. At this region the energy of the primary  $\gamma$ -ray feeding into the 596 keV state is  $E_1 = 3000 \text{ keV} - 596 \text{ keV} = 2404 \text{ keV}$  and the energy of the primary  $\gamma$ -ray feeding into the 1204 keV state is  $E_2 = 3000 \text{ keV} - 1204 \text{ keV} = 1796 \text{ keV}$ . When a plot of the data values is carried out, the strength function is decreasing as shown in figure 5.5.

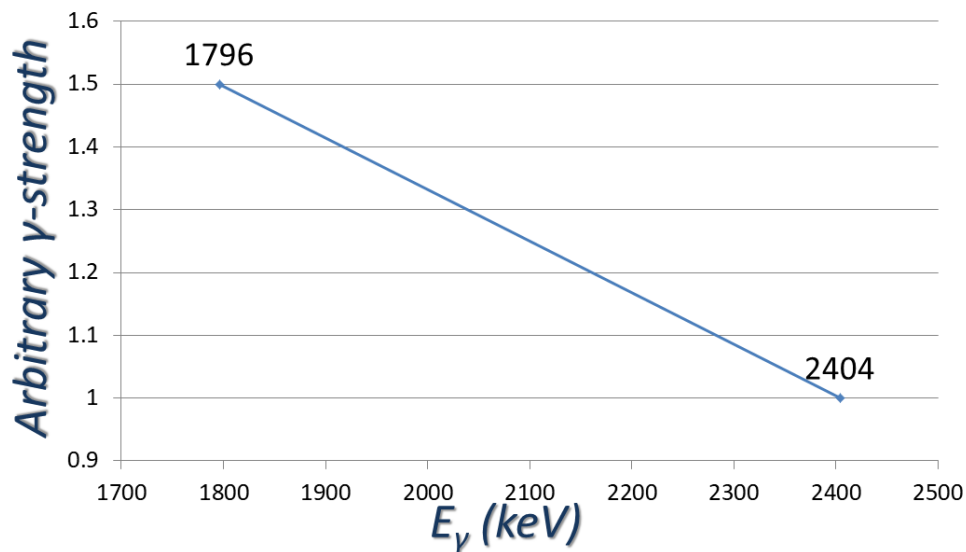


FIGURE 5.5: The shape of the strength function for  $R < 1$ .

The inverse is also true when  $R > 1$ , the relative strength function is increasing. When  $R = 1$ , the relative strength function is flat and represents the minimum of the actual GSF as shown in figure 5.4.

## 5.2 Conclusion

Figure 5.6 shows the results from the reaction  $^{74}\text{Ge}(^3\text{He}, ^3\text{He}^*)^{74}\text{Ge}$ , performed at the Oslo Cyclotron Laboratory (OCL). The lower and upper limits are a result of the systematic and statistical errors from the normalization process used. To extract the GSF of the nucleus  $^{74}\text{Ge}$  using the Oslo Method, one needs to extract the level density  $\rho(E - E_\gamma)$  and the  $\gamma$ -ray transmission coefficient  $\mathcal{J}(E_\gamma)$ . The normalization process and subsequent extraction of errors are detailed in Ref [3].

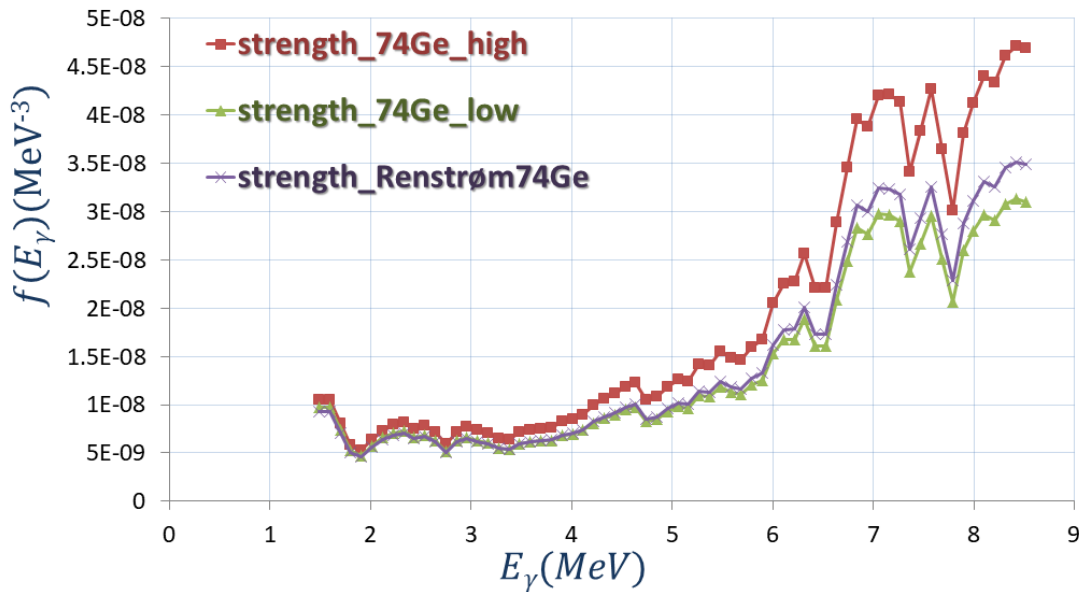


FIGURE 5.6: A plot of the data from the reaction  $^{74}\text{Ge}(^3\text{He}, ^3\text{He}^*)^{74}\text{Ge}$ , taken from Ref [3]. The actual data on the plot are represented by the purple line, the red line is the upper uncertainty limit and the green one is the lower uncertainty limit.

The figure shows the LEE at  $\gamma$ -ray energies below 4 MeV. Usually it is expected from the Lorentzian approximation of the  $\gamma$ -ray response function, that the GSF continues to decrease towards  $E = 0$ , but this is clearly not the case here. Instead there is a plateau at excitation energies below 4 MeV with what could also be an enhancement at excitation energies between 1.5-2 MeV. In the region between 7-8 MeV, a resonance-like structure is observed. This data is used with the upper and lower bounds to make a comparison with the results.

To make a comparison of the two GSF, as shown in figure 5.7, the Oslo GSF



plot was converted into a plot of  $f(596)/f(1204)$  ratios. Since the data has many resonances appearing, the data was re-binned where 3 consecutive data points next to each other were averaged to form a bin. Firstly, every primary  $\gamma$  ray was extracted on the data from 3 up to 8 MeV excitation energies.

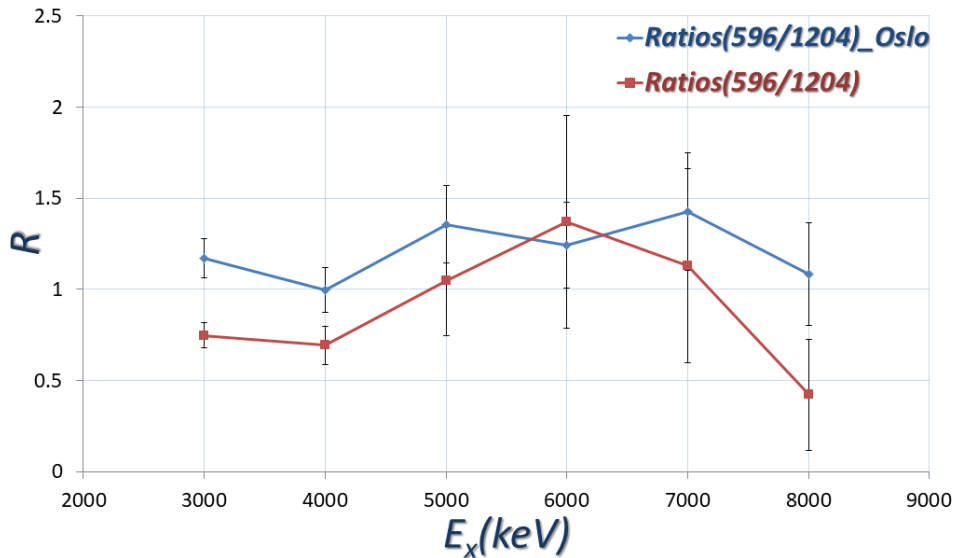


FIGURE 5.7: A plot of the data from figure 5.3 in brown and the data from figure 5.6 in blue.

From the Oslo data, the  $\gamma$  ray that decays from 3 MeV to the first-excited state, which is 596 keV, has an energy of 2404 keV. This is the first primary  $\gamma$  ray that is read from GSF to decay from 3 MeV to 596 keV level state. The same is done for the primary  $\gamma$  ray decaying to 1204 keV energy-level state. The same procedure was followed for the upper and lower bound errors of the data to determine the uncertainty range. Finally the ratio  $f(596)/f(1204)$  was taken for the Oslo data.

The two plots in figure 5.7 follow the same shape throughout as expected, but the Oslo ratio does not go below a ratio value of 1 for  $E_x < 4$  MeV, which would reflect the LEE as observed on the original plot. This is due to the fact that the data were very sensitive to resonances or nuclear structure effects in this lower-energy region which influences the ratios. Figure 5.7 also shows a large difference at  $E_x = 8$  MeV. The data shows a ratio value below 1 at 8 MeV which is not what is observed in the Oslo data in figure 5.6. The sudden decrease in the ratios at 8 MeV is due to the drop in  $\gamma$ -ray intensities, hence running out of statistics for the primary  $\gamma$  rays decaying to the 596 keV energy level as opposed to those

that decay to the 1204 keV energy level. The two data sets do seem to agree at excitation energies between 5 - 7 MeV within the error bars.

In an attempt to correct for the disagreement at low energies between the two data sets, further rebinning by 500 keV of the Oslo data was done. A polynomial fit of the form  $f(E_\gamma) = AE_\gamma^2 + BE_\gamma + C$  was applied to the data on figure 5.6 and the relative strengths of the first-excited state and the second-excited state were extracted again. The ratios of the relative strengths were taken and the result is shown in figure 5.8. There was little success in rebinning the Oslo data, but at a cost of losing too much information. The two plots agree on an increasing trend at all energies within the uncertainty except at 8 MeV as was the case in figure 5.7. The polynomial fit gives more problems than solving as it magnifies the error bars.

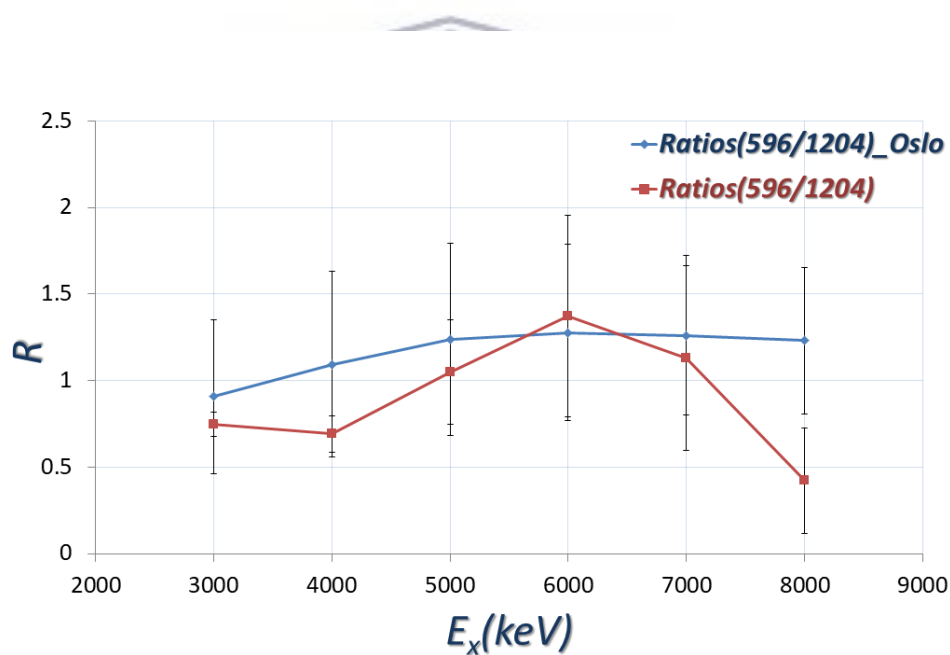


FIGURE 5.8: A plot of the data from figure 5.3 in brown and the Oslo data in blue rebinned with the use of a polynomial fit of order 2.

In conclusion, comparison of the Oslo data with these results was performed. Even though it was not possible to find a satisfactory way to compare the Oslo results with these results, the shape illustrated by the ratios from this data is consistent with the GSF extracted using the Oslo method and the LEE was also visible in the analysis. The NLD of  $^{74}\text{Ge}$  is very low as shown in figure 5.9, and as a result of that the data has very low statistics. This meant that it was not possible to take other ratios as the large error bars prohibited any meaningful analysis.

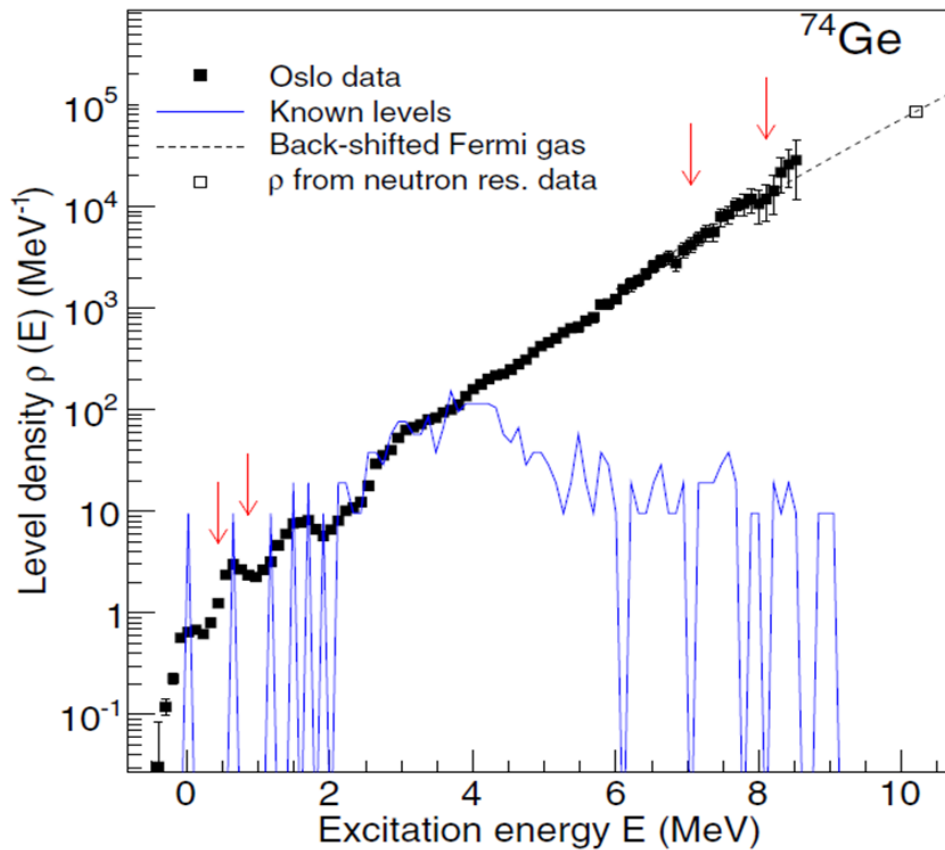


FIGURE 5.9: The experimental level density of  $^{74}\text{Ge}$  from Ref. [3]. The arrows show where the Oslo data joins the Back-shifted Fermi gas model and at the discrete energy levels.

If one was to improve and do further studies on the  $^{74}\text{Ge}$  nucleus using the same method, it would be advisable to add more  $\gamma$  ray detectors to increase statistics. In fact at iThemba LABS using the new AFRODITE array together with ALBA, which is an array of large volume  $\text{LaBr}_3$  detectors for efficient  $\gamma$ -ray detection, we can do that with high resolution and efficiency. Another solution would be to increase beam time to increase statistics.

# Bibliography

- [1] Wiedeking, M. *et al.* *Low-Energy Enhancement in the Photon Strength of  $^{95}\text{Mo}$* . Physical Review Letters 108, 162503 (2012).
- [2] Massarczyk, R. *et al.* *Dipole strength distribution of  $^{74}\text{Ge}$* . Physical Review C 92, 044309 (2015).
- [3] Renstrøm, T. *et al.* *Low-energy enhancement in the  $\gamma$ -ray strength functions of  $^{73,74}\text{Ge}$* . Physical Review C 93, 064302 (2016).
- [4] Negi, D. *et al.* *Nature of low-lying electric dipole resonance excitations in  $^{74}\text{Ge}$* . Physical Review C 94, 024332 (2016).
- [5] National Research Council. *Connecting Quarks with the Cosmos: Eleven Science Questions for the New Century*. The National Academies Press (2003).  
<http://www.fnal.gov/pub/max/pdfs/Connecting%20Quarks%20with%20the%20Cosmos.pdf>
- [6] Wiedeking, M. *(n, $\gamma$ ) cross sections for r-process nucleosynthesis*. iThemba LABS, South Africa (2015).  
[http://www.tlabs.ac.za/wp-content/uploads/pdf/rib/2015/mathis\\_wiedeking.pdf](http://www.tlabs.ac.za/wp-content/uploads/pdf/rib/2015/mathis_wiedeking.pdf)
- [7] Moore, J. W. *et al.* *University Physics*. OpenStax 3, 10 (2017).  
[https://cnx.org/resources/f5e343fdcd78d31040bafbd5e1fedf7d1fc81d5e/CNX\\_UPhysics\\_43.02\\_BindingEng.jpg](https://cnx.org/resources/f5e343fdcd78d31040bafbd5e1fedf7d1fc81d5e/CNX_UPhysics_43.02_BindingEng.jpg)
- [8] School of Physics and Astronomy. *Origin of the Heavy Elements* (2017).  
<https://www.ph.ed.ac.uk/nuclear-physics/research-activities/nuclear-astrophysics>
- [9] Burbidge, E. *et al.* *Synthesis of the Elements in Stars*. Reviews of Modern Physics 29, (547-650) (1957).  
<https://journals.aps.org/rmp/pdf/10.1103/RevModPhys.29.547>

- [10] TALYS (2017).  
<http://www.talys.eu/>
- [11] Roederer, I.U. *et al.* *Neutron-Capture Nucleosynthesis in the first stars*. The Astrophysical Journal 784, 158 (2014).  
<http://iopscience.iop.org/article/10.1088/0004-637X/784/2/158/pdf>
- [12] Schieck, H.P. *Key Nuclear Reaction Experiments: Discoveries and Consequences*. IOP Publishing (2015).
- [13] Larsen, A. C. *et al.* *Impact of a low-energy enhancement in the  $\gamma$ -ray strength function on the neutron-capture cross section*. Physical Review C 82, 014318 (2010).
- [14] Schiller, A. *et al.* Nuclear Instruments and Methods in Physics Research Section A. 447, 498 (2000).
- [15] Brink, D. M. Ph.D. thesis, Oxford University (1955).
- [16] Bartholomew, G. A. *Gamma-Ray Strength Functions*. Advances in Nuclear Physics 7, (229-324) (1973).
- [17] Bethe, H. A. Physical Review 50, 332 (1936).
- [18] Ingeberg, V. W. *Level density and  $\gamma$ -ray strength functions in  $^{87}\text{Kr}$* . MSc thesis. University of Oslo (2016).
- [19] Dilg, W. *et al.* *Level Density Parameters for the Back-Shifted Fermi Gas Model in the Mass Range  $40 < A < 250$* . Nuclear Physics A 217, (269 - 298) (1973).
- [20] Malatji, K. L. *Nuclear level densities and gamma-ray strength functions in Ta isotopes and nucleo-synthesis of  $^{180}\text{Ta}$* . MSc thesis. University of the Western Cape (2016). <http://etd.uwc.ac.za/xmlui/handle/11394/5321>
- [21] Guttormsen, M. *et al.* *Constant-temperature level densities in the quasicontinuum of Th and U isotopes*. Physical Review C 88, 024307 (2013).
- [22] Harakeh, M. N. *et al.* *Giant Resonances: Fundamental high-frequency modes of nuclear excitation*. Oxford Science Publications (2001).
- [23] Leshner, S. R. *et al.* Nuclear Instruments and Methods in Physics Research A 621, 286 (2010).

- [24] Wiedeking, M. *Low-energy enhancement of the photon strength function* (2017).  
Presentation presented at the Nuclear Spectroscopy Frontiers at Magnetic Spectrometers, Stellenbosch Institute for Advanced Studies, Stellenbosch, South Africa, November 19 - 22, 2012.
- [25] Energy Education. *Band gap* (2017).  
[http://energyeducation.ca/encyclopedia/Band\\_gap](http://energyeducation.ca/encyclopedia/Band_gap)
- [26] Micron Semiconductor Limited. *2016 Catalogue: Silicon Detectors* (2017).  
<http://www.micronsemiconductor.co.uk>
- [27] *National Nuclear Data Center* (2017).  
<https://www.nndc.bnl.gov/>
- [28]  *$^{226}\text{Ra}$  decay chain* (2017).  
[http://www.radiochemistry.org/periodictable/gamma\\_spectra/pdf/ra226.pdf](http://www.radiochemistry.org/periodictable/gamma_spectra/pdf/ra226.pdf)
- [29] Jin, H. Q. *TSCAN and Related Programs: A package to perform tape scanning and to manipulate matrices*. RUTGERS-ORNL-UTK (1997).
- [30] Milner, W. T. *Display Analysis and Manipulation Module* (1993).  
<http://www.phy.anl.gov/gammasphere/doc/damm.txt>
- [31] Ziegler, J.F. *The Stopping and Range of Ions in Matter* (2017).  
<http://www.srim.org/SRIM/SRIMINTRO.htm>
- [32] Amano, S. *et al.* Nuclear Instruments and Methods in Physics Research A. 602, 337 (2009).